INTERNATIONAL JOURNAL FOR NUMERICAL METHODS IN FLUIDS, VOL. 26, 145–175 (1998)

VARIATIONAL BOUND FINITE ELEMENT METHODS FOR THREE-DIMENSIONAL CREEPING POROUS MEDIA AND SEDIMENTATION FLOWS

MATTEO PEDERCINI,[1] ANTHONY T. PATERA[1]* AND MANUEL E. CRUZ[2]

[1]*Department of Mechanical Engineering, Massachusetts Institute of Technology, Cambridge, MA 02139, U.S.A.* [2]*Department of Mechanical Engineering, EE/COPPE/UFRJ, CP 68503, Rio de Janeiro, RJ 21945-970, Brazil*

SUMMARY

We present an analytico-computational methodology for the prediction of the effective properties of two types of three-dimensional particulate Stokes flows: porous media and sedimentation flows. In particular, we determine the permeability and average settling rate of media that consist of non-colloidal monodisperse solid spherical particles immersed in a highly viscous Newtonian fluid. Our methodology recasts the original problem into three scale-decoupled subproblems: the macro-, meso- and microscale subproblems. In the macroscale analysis the appropriate effective property is used to calculate the bulk quantity of interest. The mesoscale problem provides this effective property through the finite element solution of the transport equations in a periodic cell containing many particles distributed according to a prescribed joint probability density function. Finally, the microscale analysis allows us to accommodate mesoscale realizations in which two or more inclusions are in very close proximity; this geometrical stiffness is alleviated by introducing simple domain modifications that relax the mesh generation requirements while simultaneously yielding rigorous bounds for the effective property. Our methodology can treat random particle distributions as well as regular arrays; in the current paper we analyse only the latter. © 1998 John Wiley & Sons, Ltd.

Int. J. Numer. Meth. Fluids, **26**: 145–175 (1998)

KEY WORDS: effective property; porous media; sedimentation; finite element; Stokes flow; variational bounds

1. INTRODUCTION

Particulate flows are characterized by the motion of (solid or fluid) particles relative to a surrounding fluid. The practical importance and complex physics of such flows continue to stimulate numerous research efforts in diverse fields. However, despite recent advances in (serial and parallel) supercomputing, detailed simulation of three-dimensional particulate flows remains intractable owing to the wide range of spatial scales. As a result, there is much emphasis on modelling the macroscopic behaviour of two-phase systems as homogenized media with appropriate effective properties.

In this paper we address two types of particulate flows in which monodisperse non-colloidal solid spheres are immersed in an incompressible Newtonian fluid; creeping flow through porous media[1–3]

*Correspondence to: A. T. Patera, Room 3-266, Massachusetts Institute of Technology, 77 Massachusetts Avenue, Cambridge, MA 02139, U.S.A. Email: patera@mit.edu.

CCC 0271–2091/98/020145–31 $17.50

Received 5 February 1996
Revised 13 January 1997

and creeping (Stokes) batch sedimentation.[2–5] In the former problem the spheres are fixed in space and we determine the permeability of the material. In the latter problem we require force and torque balances for each sphere and determine the average settling speed of the suspension. In certain very special cases the two problems are effectively equivalent.

A crucial aspect of particulate flows is the underlying microstructures, characterized by the size, geometry and spatial distribution of the particles. Unfortunately, knowledge of detailed microstructures that characterize actual particulate media is scarce. In response to this uncertainty, methods have been developed which, based on very little microstructural information, provide upper and lower bounds for the permeability[6–8] and the average settling rate.[9–11] The resulting bounds can be quite crude unless high-order microstructure correlation functions are introduced,[8] but this more detailed information then complicates comparison with experimental data.[1,12]

At the other pole of effective property approaches are structure-dependent techniques, in which detailed distributional information on the phases is assumed. These approaches are relevant when the microstructure is known, can be plausibly inferred, or can be consistently calculated (as in time-dependent sedimentation approaches); the methods are also of use in 'validating' structure-independent results.[13] Purely analytical treatments of problems of the type considered in this study are primarily restricted to linear problems,[3,14] dilute concentrations,[15,16] or simple single-particle (ordered) periodic cell models.[17,18] To make further analytical progress, it is necessary to introduce simplifying, heuristic assumptions: Brinkman media,[1,19] Kynch's kinematical theory of sedimentation[20] and averaged continuum models[4] are all examples of this approach.

More recently, various computational methods have been applied to the porous media and sedimentation problems: Stokesian dynamics[21,22] and related simulation techniques[23,24] employ approximate mobility-resistance functions for particular classes of Stokes (linear) flows; serial, few-particle simulations of finite Reynolds number particulate flows have been carried out using the finite element method[25] and the finite volume method;[26] boundary integral techniques[3,27] and the boundary element method[28] have been used for parallel simulation of multiparticle creeping flow systems; and lattice gas automata[29] have been applied to the porous media problem.

In this paper we extend the variational bound (parallel Monte Carlo) finite element methodology of References 30 and 31 to study the macroscopic behaviour of *three-dimensional* creeping porous media and sedimentation flows. The approach is based on a variational hierarchical scale decomposition procedure which recasts the original multiscale problem into macro-, meso- and microscale subproblems.[30,32,33] In the macroscale problem, not treated here, an effective property (e.g. permeability) is used to calculate the bulk quantity of interest (e.g. flow rate). In the mesoscale problem[30] the effective property is determined assuming that the particles are distributed in space according to a *postulated* joint probability density function (JPDF); for random media, Monte Carlo methods are used to statistically sample the JPDF. The statistics of the original medium are captured by analysing a periodic cell of scale sufficiently large compared with a self-consistently determined correlation length.[30–32] Within this mesoscale cell the appropriate transport equations are formulated first in their strong form and, subsequently in their weak form. The latter is convenient for two reasons: first, it is the most natural for subsequent finite element discretization; second, it allows us to prove extremum principles that are useful for the microscale treatment.

Within our framework the microscale problem treats the situation in which the distance separating two or more particles is so small that numerical (finite element) solution of the corresponding mesoscale problem can be prohibitively expensive or even impossible. Such geometrical stiffness is mitigated in the microscale problem[31] by developing nip region models for particle clusters (here 'nip' region refers to the small region between close particles). In particular, our variational bound nip element procedure decomposes the geometrically stiff problem into inner (nip) and outer problems defined on the smallest and larger scales respectively. The nip region model allows the

inner problem to be solved analytically, thereby avoiding the computational difficulties associated with a large range of anisotropic scales. The inner solution is then reflected in 'coupling' boundary conditions on a now well-conditioned outer mesoscale problem in which the nip region no longer appears. Solution of the outer problem yields a rigorous upper or lower bound for the effective property of interest for a given physical nip region model; the sharpness of the bound is directly controlled by the number and extent of the excised nip regions.

The methodology described above overcomes many limitations of previous approaches. First, in the mesoscale problem we can treat many randomly distributed inclusions. Second, various shapes, sizes and distributions of particles can be considered. Third, the microscale analysis permits us to determine effective properties at *any* concentration (particle volume fraction), including maximum packing. Finally, fluid (and also particle) inertia can be incorporated into the mesoscale analysis, as carried out in References 34 and 35 for flow through fibrous (two dimensional) porous media. We emphasize that, despite the generality of the methodology, in the current paper we analyse *only* regular particle distributions, with the goal of validating our procedures for porous media and sedimentation inertia-free flows against known solutions.

The paper is organized as follows. In Section 2 the continuous formulations of the porous media and sedimentation mesoscale problems are presented. In Section 3 we develop and prove the microscale variational bounds for both problems. In Section 4 the numerical methods—mesh generation, finite element discretization and iterative solution—developed to solve the two problems are described. Finally, in Section 5 we present and discuss our results from both a numerical and a physical perspective.

2. PROBLEM FORMULATIONS

In this section we develop the mathematical formulations of the creeping porous media and sedimentation *mesoscale* problems. The formulations are applicable to both regular and random inclusion distributions.

2.1. Creeping flow through porous media

Figure 1 represents an example of a porous material in which the inclusions Ω_{di} are rigid spheres of equal diameter d held fixed in space and surrounded by a region Ω_{co} which is filled with an incompressible Newtonian fluid of density ρ_{co} and viscosity μ_{co}. The external boundaries consist of an impermeable wall Γ_{w} and inlet and outlet sections Γ_{in} and Γ_{out} where the pressures p_{in} and p_{out} are prescribed such that $\Delta P = p_{\mathrm{in}} - p_{\mathrm{out}}$. The fluid is set in motion by a pressure gradient of magnitude $\Delta P/L$ that extends over the macroscopic length scale L. We assume that the Reynolds number based on the average fluid velocity and the diameter of the spheres is sufficiently small that the fluid motion is accurately described by the incompressible Stokes equations.

Through our scale-decoupling procedure the two-phase medium is replaced with a homogeneous material with permeability κ. Through Darcy's law the macroscopic velocity (and hence volume flow rate) is related to the pressure gradient as

$$\langle \mathbf{u}_{\mathrm{orig}} \rangle_{\mathrm{v}} = -\frac{1}{\mu_{\mathrm{co}}} \boldsymbol{\kappa} \cdot \langle \nabla p_{\mathrm{orig}} \rangle_{\mathrm{v}}, \tag{1}$$

where $\mathbf{u}_{\mathrm{orig}}$ is the local fluid velocity vector on the original multicomponent domain, $\boldsymbol{\kappa}$ is the permeability tensor, ∇p_{orig} is the local pressure gradient and $\langle\ \rangle_{\mathrm{v}}$ represents volume average. We shall henceforth deal with isotropic materials only, so that a *scalar* permeability κ suffices.

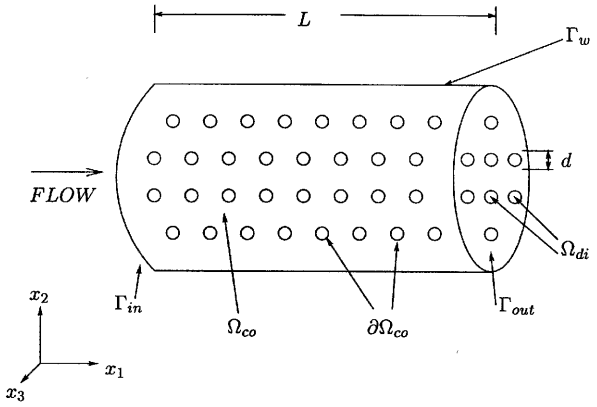

Figure 1. Example of porous medium flow: flow in a duct

The permeability is predicted by the mesoscale analysis. As shown in Figure 2, we extract a (by construction) periodic cubic cell of size λ that contains N_p spheres and solve the appropriate mesoscale Stokes equations for the velocity $\mathbf{u}(\mathbf{y})$ and the perturbation pressure $p(\mathbf{y}) \sim O(\epsilon \Delta P)$, where $\epsilon \equiv \lambda/L \ll 1$. The governing equations read[30,33,36]

$$-\frac{\partial}{\partial y_j}\left(\mu_{co}\frac{\partial u_i}{\partial y_j}\right)+\frac{\partial p}{\partial y_i}=\frac{\Delta P}{L}\delta_{1i} \quad \text{in } \Omega_{me} \quad \text{for } i=1,2,3, \tag{2}$$

$$-\frac{\partial u_i}{\partial y_i}=0 \quad \text{in } \Omega_{me}, \tag{3}$$

where δ_{ij} is the Kronecker delta symbol, Ω_{me} is the fluid region of the mesoscale cell and the summation convention over repeated indices is assumed. The no-slip Dirichlet and periodic boundary conditions are

$$\mathbf{u}=0 \quad \text{on } \partial\Omega_{me}, \tag{4}$$

and

$$\mathbf{u}(\mathbf{y})=\mathbf{u}(\mathbf{y}+\lambda(m_1\mathbf{e}_1+m_2\mathbf{e}_2+m_3\mathbf{e}_3)), \tag{5}$$

$$p(\mathbf{y})=p(\mathbf{y}+\lambda(m_1\mathbf{e}_1+m_2\mathbf{e}_2+m_3\mathbf{e}_3)), \tag{6}$$

respectively; finally, for uniqueness we require

$$\int_{\Omega_{me}} p \, d\mathbf{y}=0. \tag{7}$$

Here $(\mathbf{e}_1, \mathbf{e}_2, \mathbf{e}_3)$ are the unit vectors of the co-ordinate system (y_1, y_2, y_3), y_1 is the arbitrarily chosen direction for the driving pressure gradient, m_1, m_2 and m_3 are integers, $\partial\Omega_{me}$ represents all fluid–particle boundaries (the periodic sides of the cube, $\partial\Omega_{\#}$, are not 'real' boundaries) and $d\mathbf{y} \equiv dy_1 dy_2 dy_3$.

The permeability κ is readily derived from (1), recognizing that $\langle \nabla p_{orig} \rangle_v = -(\Delta P/L)\mathbf{e}_1$ and $\langle \mathbf{u}_{orig} \rangle_v = (1/\lambda^3)\int_{\Omega_{me}} u_1 \, d\mathbf{y} \, \mathbf{e}_1$ ($\langle u_2 \rangle_v = \langle u_3 \rangle_v = 0$ owing to isotropy). The result is

$$\kappa = \mu_{co}\frac{L}{\Delta P}\frac{1}{\lambda^3}\int_{\Omega_{me}} u_1 \, d\mathbf{y}. \tag{8}$$

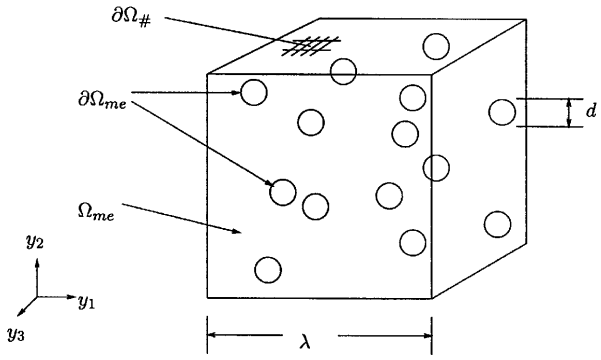

Figure 2. Mesoscale periodic (cubic) cell

As motivated in Section 1, we now pursue the variational formulation of the mesoscale problem. It can be shown[30] that the strong form (2)–(7) is equivalent to the constrained extremization problem

$$\mathbf{u} = \arg \max_{\mathbf{w} \in Z_{\Omega_{\mathrm{me}}}} J^{\mathrm{P}}_{\Omega_{\mathrm{me}}}(\mathbf{w}), \tag{9}$$

where

$$J^{\mathrm{P}}_{\Omega_{\mathrm{me}}}(\mathbf{w}) = 2\frac{\Delta P}{\mu_{\mathrm{co}} L}\int_{\Omega_{\mathrm{me}}} w_1 \, \mathrm{d}\mathbf{y} - \int_{\Omega_{\mathrm{me}}} \frac{\partial w_i}{\partial y_j}\frac{\partial w_i}{\partial y_j} \, \mathrm{d}\mathbf{y}, \tag{10}$$

$$Z_{\Omega_{\mathrm{me}}} = \{(w_1, w_2, w_3) \in (H^1_{0\#}(\Omega_{\mathrm{me}}))^3 | \mathrm{div}\ \mathbf{w} = 0\}. \tag{11}$$

Here $H^1_{0\#}(\Omega_{\mathrm{me}})$ is the space of all square-integrable functions that vanish on $\partial\Omega_{\mathrm{me}}$, are periodic (of period λ) and whose derivatives are square-integrable over Ω_{me}. By multiplying (2) by $\mathbf{u}$, integrating over Ω_{me} and using the divergence theorem along with (3), we arrive at

$$\frac{\Delta P}{\mu_{\mathrm{co}} L}\int_{\Omega_{\mathrm{me}}} u_1 \, \mathrm{d}\mathbf{y} = \int_{\Omega_{\mathrm{me}}} \frac{\partial u_i}{\partial y_j}\frac{\partial u_i}{\partial y_j} \, \mathrm{d}\mathbf{y}, \tag{12}$$

which, by virtue of (8)–(10), states that

$$\kappa = \mu^2_{\mathrm{co}} \frac{L^2}{\Delta P^2}\frac{1}{\lambda^3} \max_{\mathbf{w} \in Z_{\Omega_{\mathrm{me}}}} J^{\mathrm{P}}_{\Omega_{\mathrm{me}}}(\mathbf{w}). \tag{13}$$

The permeability is thus always non-negative and is proportional to the maximum value of the functional $J^{\mathrm{P}}_{\Omega_{\mathrm{me}}}$.

In order to arrive at the appropriate velocity field $\mathbf{u}$, we transform the constrained maximization problem (9) into an unconstrained saddle problem by introducing a Lagrange multiplier $q(\mathbf{y})$ to impose the incompressibility constraint. By taking the first variation of the resulting Lagrangian and evoking stationarity, we find that $(\mathbf{u}, p) \in \{(H^1_{0\#}(\Omega_{\mathrm{me}}))^3, L^2_{\#,0}(\Omega_{\mathrm{me}})\}$ must satisfy

$$\mu_{\mathrm{co}} \int_{\Omega_{\mathrm{me}}} \frac{\partial v_i}{\partial y_j}\frac{\partial u_i}{\partial y_j} \, \mathrm{d}\mathbf{y} - \int_{\Omega_{\mathrm{me}}} \frac{\partial v_i}{\partial y_i} p \, \mathrm{d}\mathbf{y} = \frac{\Delta P}{L}\int_{\Omega_{\mathrm{me}}} v_1 \, \mathrm{d}\mathbf{y} \quad \forall (v_1, v_2, v_3) \in (H^1_{0\#}(\Omega_{\mathrm{me}}))^3, \tag{14}$$

$$-\int_{\Omega_{\mathrm{me}}} q \frac{\partial u_i}{\partial y_i} \, \mathrm{d}\mathbf{y} = 0 \quad \forall q \in L^2_{\#,0}(\Omega_{\mathrm{me}}), \tag{15}$$

where $L^2_{\#,0}(\Omega_{\mathrm{me}})$ is the space of all λ-triply periodic functions $z(\mathbf{y})$ which are square-integrable over Ω_{me} (note that candidate pressures need not be continuous) and for which $\int_{\Omega_{\mathrm{me}}} z \, \mathrm{d}\mathbf{y} = 0$. Equations

(14) and (15) constitute the mesoscale subproblem that is solved to yield the permeability given by (8).

2.2. *Creeping sedimentation flows*

Figure 3 is a schematic diagram of particles settling under gravity in a finite closed container. As in Section 2.1, the incompressible Newtonian fluid has density ρ_{co} and viscosity μ_{co}. The particles are non-colloidal monodisperse solid spheres of diameter d and density $\rho_{di}(> \rho_{co})$ that settle under the action of gravity, $\mathbf{g} = -g\mathbf{e}_2$. We assume that inertia does not play a role in the fluid and particle motions, i.e. the motions are quasi-static. The conditions for quasi-static flow are

$$Re_p \equiv \rho_{di} V_p d/\mu_{co} \ll 1, \qquad Re_f \equiv \rho_{co} V_p l^2/\mu_{co} d \ll 1, \tag{16}$$

where Re_p and Re_f are the particle and fluid Reynolds numbers respectively, V_p is the Stokes settling speed of a single particle in an unbounded fluid and l is the characteristic interparticle distance. The two conditions of (16) are equivalent to requiring that both the particle and fluid characteristic equilibrium times be much less than d/V_p; the former can be estimated as $d^2\rho_{di}/\mu_{co}$ and the latter as $l^2\rho_{co}/\mu_{co}$. The quasi-static assumption allows us to replace the self-consistent motion of the suspension with a JPDF that we sample by taking 'snapshots' of the system, as originally proposed by Batchelor.[15]

As shown in Figure 3, a suspension sedimenting in a container creates three distinct regions of different particle concentration: the upper clarified region consisting of fluid with no particles, the lower compression zone in which the particles accumulate and the middle region or suspension zone. We focus our attention on the latter region. Note that since the settling process occurs in a closed tank, we require zero net (fluid and particle) volume flow rate at any horizontal surface.[4,15,20]

Our homogeneous, quasi-static, quantity of interest is the average sedimentation speed (or settling rate) $\mathscr{U}$. Since this quantity defines our macroscale subproblem, we pass directly to the mesoscale formulation. It should be noted that for other suspension flows, e.g. duct flows,[37] the macroscale problem is much more complex.

The mesoscale problem yields the average settling speed $\mathscr{U}$. As in Figure 2, we extract a (by construction) periodic cell of size λ that contains N_p spheres. In what follows, we allow for spheres of different diameters, since the upper-bound microscale treatment involves a bidisperse suspension (see Section 3.2.2). On the mesoscale the pressure can be written as $p = p_0 - \rho_{co} g y_2 - \tau y_2 + p'(\mathbf{y})$; here p_0 is a reference pressure, $g(> 0)$ is the acceleration due to gravity, τ is the (positive) fluid 'backflow' pressure gradient and $p'(\mathbf{y})$ is the periodic perturbation pressure. The 'backflow' pressure gradient is determined from the zero-volume-flow-rate condition and can be viewed as the pressure gradient responsible for the upward movement of fluid as the particles settle.

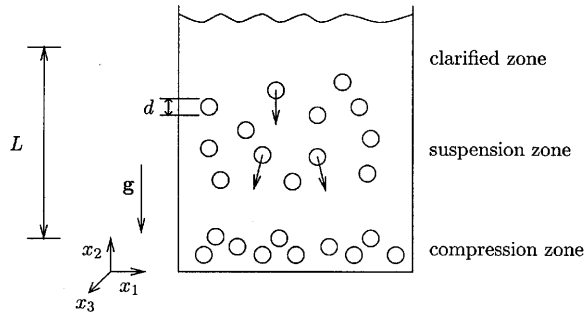

Figure 3. Batch particle Stokes sedimentation

The mesoscale equations of fluid motion are

$$-\frac{\partial}{\partial y_j}\left[\mu_{\mathrm{co}}\left(\frac{\partial u_i}{\partial y_j}+\frac{\partial u_j}{\partial y_i}\right)\right]+\frac{\partial p'}{\partial y_i}-\tau\delta_{2i}=0 \quad \text{in } \Omega_{\mathrm{me}} \quad \text{for } i=1,2,3, \tag{17}$$

$$-\frac{\partial u_i}{\partial y_i}=0 \quad \text{in } \Omega_{\mathrm{me}}. \tag{18}$$

Turning to the boundary conditions, the velocity and (perturbation) pressure fields must be λ-triply periodic and the no-slip condition must be consistent with solid body rotation and translation of each particle. In addition, the quasi-static assumption requires zero net force and torque on each particle. Mathematically, these conditions read

$$\mathbf{u}|_{\partial\Omega_k}=\mathbf{U}_k+\mathbf{R}_k\times(\mathbf{y}-\mathbf{y}_k), \quad k=1,\ldots,N_{\mathrm{p}}, \tag{19}$$

$$\int_{\partial\Omega_k}(\mathbf{T}'\cdot\mathbf{n})\,\mathrm{d}s=(\tau\mathscr{V}_k-\mathscr{W}_k)\mathbf{e}_2, \quad k=1,\ldots,N_{\mathrm{p}}, \tag{20}$$

$$\int_{\partial\Omega_k}(\mathbf{y}-\mathbf{y}_k)\times(\mathbf{T}'\cdot\mathbf{n})\,\mathrm{d}s=0, \quad k=1,\ldots,N_{\mathrm{p}}, \tag{21}$$

where $\partial\Omega_k$ is the surface of sphere k, $\mathbf{U}_k$ and $\mathbf{R}_k$ are respectively the translational and rotational velocity vectors of particle k, $(\,)\times(\,)$ denotes the cross-product, $\mathbf{y}_k$ denotes the centre (and centre of mass) of particle k, $T'_{ij}=\mu_{\mathrm{co}}(\partial u_i/\partial y_j+\partial u_j/\partial y_i)-p'\delta_{ij}$ is the 'perturbation' stress tensor, $(\mathbf{T}'\cdot\mathbf{n})=T'_{ij}n_j$ (where n_j is the outward normal from Ω_{me} on $\partial\Omega_{\mathrm{me}}$), $\mathrm{d}s$ is an infinitesimal surface element, $\mathscr{V}_k$ is the volume of particle k and $\mathscr{W}_k=\mathscr{V}_k(\rho_{\mathrm{di}}-\rho_{\mathrm{co}})g$ is the buoyancy-corrected weight of particle k. Finally, we must require the zero-net-flow-rate condition

$$-\left(\int_{\Omega_{\mathrm{me}}}u_2\,\mathrm{d}\mathbf{y}+\sum_{k=1}^{N_{\mathrm{p}}}\mathscr{V}_k(U_2)_k\right)=0, \tag{22}$$

as well as

$$\int_{\Omega_{\mathrm{me}}}u_1\,\mathrm{d}\mathbf{y}=\int_{\Omega_{\mathrm{me}}}u_3\,\mathrm{d}\mathbf{y}=0, \tag{23}$$

$$\int_{\Omega_{\mathrm{me}}}p'\,\mathrm{d}\mathbf{y}=0 \tag{24}$$

for uniqueness.

We make two remarks. First, instead of the usual Laplacian operator for the viscous term in (17), we use an equivalent 'stress formulation' which will allow us to incorporate the stress boundary conditions (20) and (21) naturally in the variational weak form. Second, we note that τ and $(\mathbf{U}_k,\mathbf{R}_k)$ are not specified but rather are part of the solution. In essence, equations (20)–(22) are the complementary conditions from which the particle velocities and the backflow pressure gradient can be deduced. The strong-form equations (17)–(24) are the point of departure for Batchelor's analysis.[15]

In the sedimentation problem the effective property of interest is the average settling speed of the particles, which, by virtue of horizontal (x_1-x_3 plane) homogeneity, is defined as

$$\mathscr{U}\equiv\frac{1}{\sum_{k=1}^{N_p}\mathscr{W}_k}I^{\mathrm{S}}_{\Omega_{\mathrm{me}}}(\mathbf{u}), \tag{25}$$

where, for velocity fields $\mathbf{w}$ satisfying $\mathbf{w}|_{\partial\Omega_k} = \mathbf{W}_k + \mathbf{Z}_k \times (\mathbf{y} - \mathbf{y}_k)$,

$$I^{\mathrm{S}}_{\Omega_{\mathrm{me}}}(\mathbf{w}) = -\sum_{k=1}^{N_{\mathrm{p}}} \mathscr{W}_k (W_2)_k. \tag{26}$$

We also introduce the functional $J^{\mathrm{S}}_{\Omega_{\mathrm{me}}}(\mathbf{w})$,

$$J^{\mathrm{S}}_{\Omega_{\mathrm{me}}}(\mathbf{w}) = 2I^{\mathrm{S}}_{\Omega_{\mathrm{me}}}(\mathbf{w}) - \mu_{\mathrm{co}} \frac{1}{2} \int_{\Omega_{\mathrm{me}}} \left(\frac{\partial w_i}{\partial y_j} + \frac{\partial w_j}{\partial y_i} \right) \left(\frac{\partial w_i}{\partial y_j} + \frac{\partial w_j}{\partial y_i} \right) \mathrm{d}\mathbf{y}, \tag{27}$$

the second term of which we shall denote the *dissipation integral*. By multiplying equation (17) by $\mathbf{u}$, integrating by parts over Ω_{me} and using (18)–(22), we derive[33]

$$I^{\mathrm{S}}_{\Omega_{\mathrm{me}}}(\mathbf{u}) = J^{\mathrm{S}}_{\Omega\mathrm{me}}(\mathbf{u}) = \mu_{\mathrm{co}} \frac{1}{2} \int_{\Omega_{\mathrm{me}}} \left(\frac{\partial u_i}{\partial y_j} + \frac{\partial u_j}{\partial y_i} \right) \left(\frac{\partial u_i}{\partial y_j} + \frac{\partial u_j}{\partial y_i} \right) \mathrm{d}\mathbf{y}. \tag{28}$$

From (25) and (28) it is clear that the average settling velocity $\mathscr{U}$ is always positive.

As in the porous media case (Section 2.1), we recast the problem in variational form to implement the microscale treatment and the finite element method. We can prove that[33]

$$\mathbf{u} = \arg \max_{\mathbf{w} \in B_{\Omega_{\mathrm{me}}}} J^{\mathrm{S}}_{\Omega_{\mathrm{me}}}(\mathbf{w}), \tag{29}$$

where

$$B_{\Omega_{\mathrm{me}}} = \{\mathbf{w} \in Y(\Omega_{\mathrm{me}}) | \mathrm{div}\ \mathbf{w} = 0, \int_{\Omega_{\mathrm{me}}} w_2\ \mathrm{d}\mathbf{y} + \sum_{k=1}^{N_{\mathrm{p}}} \mathscr{V}_k (W_2)_k = 0\}, \tag{30}$$

$$Y(\Omega_{\mathrm{me}}) = \Bigg\{ (w_1, w_2, w_3) \in (H^1_{\#}(\Omega_{\mathrm{me}}))^3 | \int_{\Omega_{\mathrm{me}}} w_1\ \mathrm{d}\mathbf{y} = 0, \int_{\Omega_{\mathrm{me}}} w_3\ \mathrm{d}\mathbf{y} = 0,$$

$$\text{and } \forall k \in \{1, \ldots, N_{\mathrm{p}}\}, \mathbf{w}|_{\partial\Omega_k} = \mathbf{W}_k + \mathbf{Z}_k \times (\mathbf{y} - \mathbf{y}_k), \mathbf{W}_k \in \mathscr{R}^3, \mathbf{Z}_k \in \mathscr{R}^3 \Bigg\}, \tag{31}$$

and $\mathscr{R}$ is the set of real numbers. From (25), (28) and (29) we can derive the following expression for the settling velocity:

$$\mathscr{U} = \frac{1}{\sum_{k=1}^{N_{\mathrm{p}}} \mathscr{W}_k} \max_{\mathbf{w} \in B_{\Omega_{\mathrm{me}}}} J^{\mathrm{S}}_{\Omega_{\mathrm{me}}}(\mathbf{w}). \tag{32}$$

Related variational expressions for the sedimentation problem can be found in References 9, 10 and 3; related extremum statements for the settling velocity can be found in Reference 10. In order to arrive at (29) and hence (32), we multiply (17) by the test function $\mathbf{v} \in B_{\Omega_{\mathrm{me}}}$ and integrate over Ω_{me}. We then integrate by parts and use (20), (21) and the attributes of the space $B_{\Omega_{\mathrm{me}}}$ to demonstrate that the first variation of $J^{\mathrm{S}}_{\Omega_{\mathrm{me}}}(\mathbf{u})$ vanishes $\forall \mathbf{v} \in B_{\Omega_{\mathrm{me}}}$. As the functional $J^{\mathrm{S}}_{\Omega_{\mathrm{me}}}(\mathbf{w})$ is negative definite, (29) directly follows.[33]

As in the previous section, we now convert the constrained maximization problem into an unconstrained extremization problem by introducing two Lagrange multipliers: $q(\mathbf{y}) \in L^2_{\#,0}(\Omega_{\mathrm{me}})$ to impose the incompressibility constraint and $\eta \in \mathscr{R}$ to impose the zero-volume-flow-rate constraint.

Requiring stationarity, we find that $(\mathbf{u}, p', \tau) \in (Y(\Omega_{\mathrm{me}}), L^2_{\#,0}(\Omega_{\mathrm{me}}), \mathscr{R})$ must satisfy the variational weak form

$$\mu_{\mathrm{co}} \int_{\Omega_{\mathrm{me}}} \frac{\partial v_i}{\partial y_j}\left(\frac{\partial u_i}{\partial y_j}+\frac{\partial u_j}{\partial y_i}\right) \mathrm{d}\mathbf{y} - \int_{\Omega_{\mathrm{me}}} p' \frac{\partial v_i}{\partial y_i}\, \mathrm{d}\mathbf{y} - \tau\left(\int_{\Omega_{\mathrm{me}}} v_2\, \mathrm{d}\mathbf{y} + \sum_{k=1}^{N_{\mathrm{p}}} \mathscr{V}_k (V_2)_k\right) = I^{\mathrm{S}}_{\Omega_{\mathrm{me}}}(\mathbf{v}) \quad \forall \mathbf{v} \in Y(\Omega_{\mathrm{me}}), \tag{33}$$

$$-\int_{\Omega_{\mathrm{me}}} q \frac{\partial u_i}{\partial y_i}\, \mathrm{d}\mathbf{y} = 0 \quad \forall q \in L^2_{\#,0}(\Omega_{\mathrm{me}}), \tag{34}$$

$$-\eta\left(\int_{\Omega_{\mathrm{me}}} u_2\, \mathrm{d}\mathbf{y} + \sum_{k=1}^{N_{\mathrm{p}}} \mathscr{V}_k (U_2)_k\right) = 0 \quad \forall \eta \in \mathscr{R}. \tag{35}$$

It is readily shown that the form (33)–(35) is equivalent to the strong form (17)–(24). Indeed, multiplying (17) by $\mathbf{v} \in Y(\Omega_{\mathrm{me}})$ and integrating by parts over Ω_{me}, we obtain (33); similarly, multiplying (18) by $q \in L^2_{\#,0}$ and integrating over Ω_{me}, we obtain (34); lastly, (35) results from multiplying (22) by $\eta \in \mathscr{R}$. It is important to observe that the zero-net-force and zero-torque requirements of (20) and (21) appear as *natural* boundary conditions in the variational formulation of the sedimentation problem. This constitutes a great advantage for subsequent numerical implementation.

Note that if we choose $\mathbf{v} = (0, 1, 0) \in Y(\Omega_{\mathrm{me}})$, we derive from (33) that

$$\tau = \frac{\sum_{k=1}^{N_{\mathrm{p}}} \mathscr{W}_k}{\mathscr{V}_{\mathrm{tot}}}, \tag{36}$$

where $\mathscr{V}_{\mathrm{tot}} = (\sum_{k=1}^{N_{\mathrm{p}}} \mathscr{V}_k + \int_{\Omega_{\mathrm{me}}} \mathrm{d}\mathbf{y}) = \lambda^3$ is the total volume of the mesoscale cell. Although one of the unknowns of the problem has been determined, it can be seen that we do not have more independent equations than unknowns. In particular, equations (33) and (34) yield $\mathbf{u}$ only to within a constant; it is through the application of (35) that the velocity is rendered unique. Physically, equation (36) shows that the backflow pressure gradient τ depends only on the buoyancy-corrected weight and concentration of the particles, not on their spatial distribution. This can be understood by carrying out a y_2-momentum balance for a control volume that consists of the entire mesoscale cell. It is clear that the hydrostatic pressure distribution balances the weight of the fluid and is responsible for the buoyancy forces on the particles; the only other force that can balance the buoyancy-corrected weight of the particles, $\sum_{k=1}^{N_{\mathrm{p}}} \mathscr{W}_k$, is therefore $\tau \mathscr{V}_{\mathrm{tot}}$.

3. MICROSCALE VARIATIONAL BOUNDS

As discussed earlier, our mesoscale analysis may be hindered by the close proximity of two or more spheres. In order to circumvent the problem, a variational bound methodology is pursued in which we introduce geometric modifications that improve the conditioning of the problem while simultaneously yielding bounds for the effective property of interest. The proofs are based on the extremizing properties of the scalar permeability κ and the average settling speed $\mathscr{U}$ and rely on standard variational techniques of space restriction and expansion.[3,9,10] Although the proofs presented are for a single nip region in an N-sphere mesoscale cell, the results are readily extended to multiple nips.[31] Note that our microscale analysis is not intended to approximate the fluid flow in the nip region; rather, it is designed to provide reasonably sharp bounds on the macroscopic scale (i.e. for the effective property).

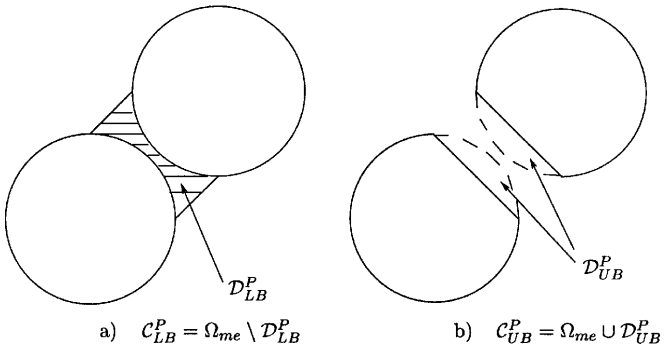

Figure 4. Porous media nip region modifications: (a) nip region blockage (lower bound); (b) nip region enlargement (upper bound)

3.1. Porous media problem

Figure 4 shows the simple geometric modifications proposed for the porous media case. To obtain a lower bound, the two spheres are connected with a solid cylinder whose axis coincides with the line of centres (Figure 4(a)). The modified fluid region $\mathscr{C}^{\mathrm{P}}_{\mathrm{LB}}$ is now the original fluid region Ω_{me} minus the nip region $\mathscr{D}^{\mathrm{P}}_{\mathrm{LB}}(\mathscr{C}^{\mathrm{P}}_{\mathrm{LB}} = \Omega_{\mathrm{me}} \backslash \mathscr{D}^{\mathrm{P}}_{\mathrm{LB}})$. Figure 4(b) depicts the upper-bound geometry, which consists of two 'shaved' spheres. In this case the fluid region $\mathscr{C}^{\mathrm{P}}_{\mathrm{UB}}$ occupies region $\mathscr{D}^{\mathrm{P}}_{\mathrm{UB}}$ as well as the domain $\Omega_{\mathrm{me}}(\mathscr{C}^{\mathrm{P}}_{\mathrm{UB}} = \Omega_{\mathrm{me}} \cup \mathscr{D}^{\mathrm{P}}_{\mathrm{UB}})$. The porous media proofs follow the arguments in Reference 31 for two-dimensional porous media (i.e. cylinders in a cross-flow), which we briefly recall.

3.1.1. Lower bound. Physically, the lower bound is achieved by blocking the flow between selected particle pairs; mathematically, the proof is based on variational arguments. We define three motions as shown in Figure 5: motion 1 corresponds to the solution of the original geometrically stiff porous media problem over the fluid region Ω_{me}; motion 2 corresponds to the solution over the modified geometry $\mathscr{C}^{\mathrm{P}}_{\mathrm{LB}}$; and motion 3 corresponds to the velocity field of motion 2 extended to the geometry of motion 1, such that we remove region $\mathscr{D}^{\mathrm{P}}_{\mathrm{LB}}$ and replace it with fluid at rest. To show that the permeability of motion 2 is a lower bound, we present two intermediate results. First, it is readily shown that the velocity field of motion 3 is an admissible (though presumably non-maximizing) candidate to the porous media variational statement (9) defined over region Ω_{me}. Second, motions 2

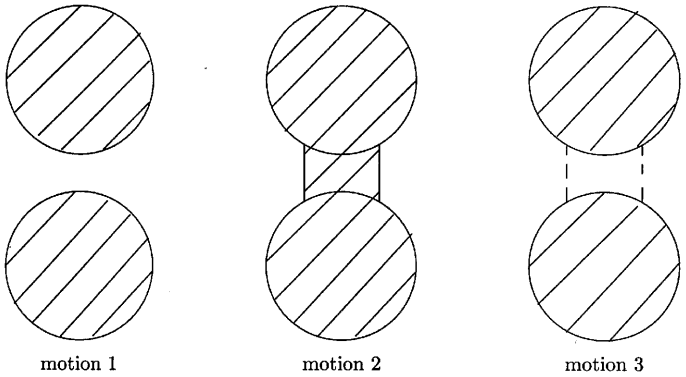

Figure 5. Motions for porous media and sedimentation lower-bound proofs

and 3 produce the same value for the functional $J^{\mathrm{P}}_{\Omega_{\mathrm{me}}}$, since the quiescent fluid that replaces region $\mathscr{D}^{\mathrm{P}}_{\mathrm{LB}}$ in motion 3 does not contribute to the integrals. Mathematically, the two results read

$$J^{\mathrm{P}}_{\Omega_{\mathrm{me}}}(\mathbf{u}^{(1)}) \geqslant J^{\mathrm{P}}_{\Omega_{\mathrm{me}}}(\mathbf{u}^{(3)}), \tag{37}$$

$$J^{\mathrm{P}}_{\mathscr{C}^{\mathrm{P}}_{\mathrm{LB}}}(\mathbf{u}^{(2)}) = J^{\mathrm{P}}_{\Omega_{\mathrm{me}}}(\mathbf{u}^{(3)}), \tag{38}$$

where $\mathbf{u}^{(n)}$ is the velocity field of motion $n = 1, 2, 3$. Here (37) follows from the fact that $\mathbf{u}^{(3)} \in Z_{\Omega_{\mathrm{me}}}$ as defined in (11). From (37), (38) and the extremum statement of (13) we can write

$$\kappa = \mu^2_{\mathrm{co}} \frac{L^2}{\Delta P^2} \frac{1}{\lambda^3} J^{\mathrm{P}}_{\Omega_{\mathrm{me}}}(\mathbf{u}^{(1)}) \geqslant \mu^2_{\mathrm{co}} \frac{L^2}{\Delta P^2} \frac{1}{\lambda^3} J^{\mathrm{P}}_{\Omega_{\mathrm{me}}}(\mathbf{u}^{(3)}) = \mu^2_{\mathrm{co}} \frac{L^2}{\Delta P^2} \frac{1}{\lambda^3} J^{\mathrm{P}}_{\mathscr{C}^{\mathrm{P}}_{\mathrm{LB}}}(\mathbf{u}^{(2)}) \equiv \kappa_{\mathrm{LB}}, \tag{39}$$

which is the desired result. It can be further shown that by decreasing the radius of the nip region, a sharper bound is obtained.

3.1.2. Upper bound. The physical argument in favour of the proposed nip enlargement technique is that the new geometry enhances the flow through the nip. As for the lower-bound proof, we introduce three motions as shown in Figure 6: motion 1 consists of the solution of the original mesoscale problem in region Ω_{me}; motion 2 is the solution of the porous media problem over the enlarged geometery $\mathscr{C}^{\mathrm{P}}_{\mathrm{UB}} = \Omega_{\mathrm{me}} \cup \mathscr{D}^{\mathrm{P}}_{\mathrm{UB}}$; motion 3 consists of the fluid region $\mathscr{C}^{\mathrm{P}}_{\mathrm{UB}}$ with the velocity field of motion 1 extended to include the nip region $\mathscr{D}^{\mathrm{P}}_{\mathrm{UB}}$, which is thus filled with quiescent fluid. Similarly to Section 3.1.1, we thus have

$$J^{\mathrm{P}}_{\mathscr{C}^{\mathrm{P}}_{\mathrm{UB}}}(\mathbf{u}^{(2)}) \geqslant J^{\mathrm{P}}_{\mathscr{C}^{\mathrm{P}}_{\mathrm{UB}}}(\mathbf{u}^{(3)}), \tag{40}$$

$$J^{\mathrm{P}}_{\Omega_{\mathrm{me}}}(\mathbf{u}^{(1)}) = J^{\mathrm{P}}_{\mathscr{C}^{\mathrm{P}}_{\mathrm{UB}}}(\mathbf{u}^{(3)}), \tag{41}$$

where (40) follows from $\mathbf{u}^{(3)} \in Z_{\mathscr{C}^{\mathrm{P}}_{\mathrm{UB}}}$. From (40), (41) and the extremum statement of (13) we obtain

$$\kappa = \mu^2_{\mathrm{co}} \frac{L^2}{\Delta P^2} \frac{1}{\lambda^3} J^{\mathrm{P}}_{\Omega_{\mathrm{me}}}(\mathbf{u}^{(1)}) = \mu^2_{\mathrm{co}} \frac{L^2}{\Delta P^2} \frac{1}{\lambda^3} J^{\mathrm{P}}_{\mathscr{C}^{\mathrm{P}}_{\mathrm{UB}}}(\mathbf{u}^{(3)}) \leqslant \mu^2_{\mathrm{co}} \frac{L^2}{\Delta P^2} \frac{1}{\lambda^3} J^{\mathrm{P}}_{\mathscr{C}^{\mathrm{P}}_{\mathrm{UB}}}(\mathbf{u}^{(2)}) \equiv \kappa_{\mathrm{UB}}, \tag{42}$$

which is the desired result. Again by decreasing the size of region $\mathscr{D}^{\mathrm{P}}_{\mathrm{UB}}$ for a given mesoscale geometry, the upper bound becomes sharper.

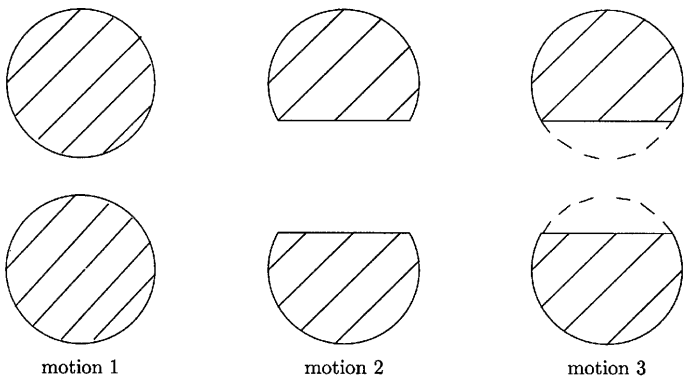

Figure 6. Motions for porous media upper-bound proof

3.2. Sedimentation problem

As shown in Figure 7, the geometries of the proposed microscale models are simple. Figure 7(a) is a sketch of the lower-bound geometry, which is obtained by rigidly connecting a pair of spheres by means of a *neutrally* buoyant cylinder $\mathscr{D}^{\mathrm{S}}_{\mathrm{LB}}$ whose axis coincides with the line of centres and whose spherical end-caps are removed. Figure 7(b) shows the upper-bound geometry, which is obtained by reducing the diameter of the spheres while holding their centres $\mathbf{y}_k$ in the same location and increasing their density to conserve their original buoyancy-corrected weights $\mathscr{W}_k$. We shall denote the number of spheres in the original system as N.

3.2.1. Lower bound. Figure 5 shows the pair of modified spheres for three different mesoscale motions. Motion 1 is the original motion of the $N_{\mathrm{p}} = N$ sedimenting spheres in the fluid region Ω_{me}. Motion 2 consists of the motion of $N_{\mathrm{p}} = N - 1$ sedimenting particles, one of which is the 'dumb-bell' obtained by connecting two 'selected' particles from the original configuration; the fluid occupies region $\mathscr{C}^{\mathrm{S}}_{\mathrm{LB}} = \Omega_{\mathrm{me}} \backslash \mathscr{D}^{\mathrm{S}}_{\mathrm{LB}}$. Lastly, motion 3 is the 'dumb-bell' motion 2 extended to the larger fluid domain Ω_{me} of motion 1. The proof follows the same logic as the porous media lower-bound proof. However, owing to the additional particle dynamics, we present a more detailed derivation.[33] We first consider each velocity field $\mathbf{u}^{(n)}$, $n = 1, 2, 3$; we then relate the corresponding functionals $J^{\mathrm{S}}(\mathbf{u}^{(n)})$.

Motion 1 is characterized by the fluid velocity $\mathbf{u}^{(1)}$ which satisfies equations (17)–(24) over region Ω_{me}, with $N_{\mathrm{p}} = N$, $\mathscr{V}_k = \pi d^3/6$, $\mathscr{W}_k = \mathscr{W} \equiv \mathscr{V}_k(\rho_{\mathrm{di}} - \rho_{\mathrm{co}})g$, $k = 1, \ldots, N_{\mathrm{p}}$. From (29), motion 1 is such that

$$\mathbf{u}^{(1)} = \arg \max_{\mathbf{w} \in B_{\Omega_{\mathrm{me}}}} J^{\mathrm{S}}_{\Omega_{\mathrm{me}}}(\mathbf{w}), \tag{43}$$

with associated settling speed given by (32), which we can rewrite as

$$\mathscr{U}^{(1)} = \frac{1}{N\mathscr{W}} J^{\mathrm{S}}_{\Omega_{\mathrm{me}}}(\mathbf{u}^{(1)}), \tag{44}$$

since all particles are of the same weight.

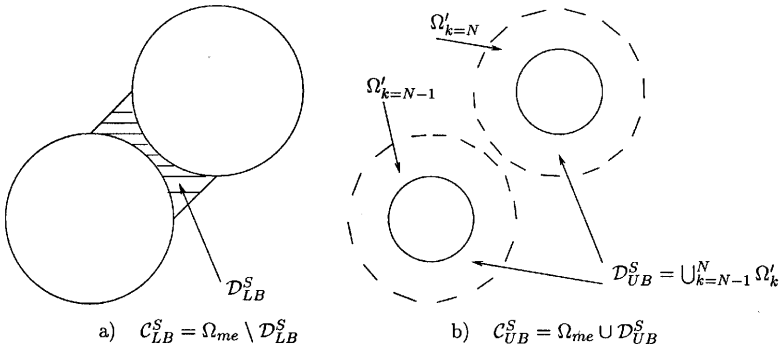

Figure 7. Sedimentation nip region modifications: (a) connecting two spheres to make a dumb-bell (lower bound); (b) shrinking two spheres (upper bound)

In motion 2 we treat the two particles that make up the 'dumb-bell' as a single particle with buoyancy-corrected weight $2\mathscr{W}$. The buoyancy-corrected weight $\mathscr{W}_k$ and the volume $\mathscr{V}_k$ of particle k are thus given by

$$\mathscr{W}_k = \begin{cases} \mathscr{W} & \text{if } k = 1, \ldots, N_D - 1, \\ 2\mathscr{W} & \text{if } k = N_D, \end{cases} \tag{45}$$

$$\mathscr{V}_k = \begin{cases} (\pi/6)d^3 & \text{if } k = 1, \ldots, N_D - 1, \\ 2(\pi/6)d^3 + \mathscr{V}_{nip} & \text{if } k = N_D, \end{cases} \tag{46}$$

where $N_D = N_p = N - 1$ is the number of particles in motion 2, $k = N_D$ represents the dumb-bell (with no loss of generality) and $\mathscr{V}_{nip}$ is the volume of the nip region $\mathscr{D}^S_{LB}$. In the proofs that follow, it is important to note that the centre of gravity of the dumb-bell, $\mathbf{y}_{N_D}$, is located at the midpoint of the segment connecting the centres of the two constituent spheres. As for the original sedimentation problem (see Section 2.2), we can then prove that

$$\mathbf{u}^{(2)} = \arg \max_{\mathbf{w} \in B_{\mathscr{C}^S_{LB}}} J^S_{\mathscr{C}^S_{LB}}(\mathbf{w}) \tag{47}$$

and define

$$\mathscr{U}^{(2)} = \frac{1}{N\mathscr{W}} J^S_{\mathscr{C}^S_{LB}}(\mathbf{u}^{(2)}), \tag{48}$$

where $\mathscr{U}^{(2)}$ is the settling speed for motion 2. Note that as an alternative approach, equation (48) can be derived from equation (25) by replacing Ω_{me} with $\mathscr{C}^S_{LB}$.

Finally, in motion 3 the fluid region of motion 2 is enlarged to contain the nip region $\mathscr{D}^S_{LB}$ (N_p is again N), with a velocity field that consists of $\mathbf{u}^{(2)}$ extended to region $\mathscr{D}^S_{LB}$:

$$\mathbf{u}^{(3)} = \begin{cases} \mathbf{u}^{(2)} - A\mathbf{e}_1 - C\mathbf{e}_3 & \text{in } \Omega_{me} \backslash \mathscr{D}^S_{LB}, \\ \mathbf{U}^{(2)}_{N_D} + \mathbf{R}^{(2)}_{N_D} \times (\mathbf{y} - \mathbf{y}_{N_D}) - A\mathbf{e}_1 - C\mathbf{e}_3 & \text{in } \mathscr{D}^S_{LB}, \end{cases} \tag{49}$$

where $\mathbf{U}^{(2)}_{N_D}$ and $\mathbf{R}^{(2)}_{N_D}$ are the dumb-bell translational and rotational velocities respectively, $A = (\mathscr{V}_{nip}/\mathscr{V}_{\Omega_{me}})(U^{(2)}_1)_{N_D}$ and $C = (\mathscr{V}_{nip}/\mathscr{V}_{\Omega_{me}})(U^{(2)}_3)_{N_D}$ are shifts introduced to satisfy the horizontal homogeneity constraints of (31) over region Ω_{me} and $\mathscr{V}_{\Omega_{me}}$ is the volume of region Ω_{me}. Note that by construction the backflow pressure gradient $\tau = N\mathscr{W}/\lambda^3$ is the same for all three motions.

Having described the three motions, we first claim that

$$J^S_{\Omega_{me}}(\mathbf{u}^{(1)}) \geqslant J^S_{\Omega_{me}}(\mathbf{u}^{(3)}), \tag{50}$$

since $\mathbf{u}^{(3)} \in B_{\Omega_{me}}$ and $\mathbf{u}^{(1)}$ is the argument that maximizes $J^S_{\Omega_{me}}$ as described in (43). To verify that $\mathbf{u}^{(3)} \in B_{\Omega_{me}}$, we note that: $\mathbf{u}^{(3)}$ satisfies (23) by construction; $\mathbf{u}^{(3)}$ satisfies the zero-net-volume-flow-rate condition (22)—what the solid 'loses' is regained by the fluid; $\mathbf{u}^{(3)}$ is continuous and λ-triply periodic (i.e. is in $(H^1_{\#}(\Omega_{me}))^3$); $\mathbf{u}^{(3)}$ is consistent with solid body motion at the particle surfaces, i.e. satisfies the no-slip boundary condition; and $\mathbf{u}^3$ is divergence-free, since the fluid in region $\mathscr{D}^S_{LB}$ is in solid body motion.

Next we note that the velocity fields of motions 2 and 3 produce the same value of the dissipation integral, since solid body rotation and translation of the fluid in region $\mathscr{D}^S_{LB}$ of motion 3 do not contribute to this integral. Then, since $I^S_{\mathscr{C}^S_{LB}}(\mathbf{u}^{(2)}) = I^S_{\Omega_{me}}(\mathbf{u}^{(3)})$, we must have

$$J^S_{\mathscr{C}^S_{LB}}(\mathbf{u}^{(2)}) = J^S_{\Omega_{me}}(\mathbf{u}^{(3)}). \tag{51}$$

Finally, from (44), (50), (51) and (48) we can assert that

$$\mathscr{U} = \mathscr{U}^{(1)} = \frac{1}{N\mathscr{W}} J^{\mathrm{S}}_{\Omega_{\mathrm{me}}}(\mathbf{u}^{(1)}) \geqslant \frac{1}{N\mathscr{W}} J^{\mathrm{S}}_{\Omega_{\mathrm{me}}}(\mathbf{u}^{(3)}) = \frac{1}{N\mathscr{W}} J^{\mathrm{S}}_{\mathscr{C}^{\mathrm{S}}_{\mathrm{LB}}}(\mathbf{u}^{(2)}) = \mathscr{U}^{(2)} \equiv \mathscr{U}_{\mathrm{LB}}, \tag{52}$$

as desired.

3.2.2. Upper bound. The upper-bound proof follows closely that of the lower bound. Figure 8 shows three different motions. Motion 1 is the original motion of the $N_{\mathrm{p}} = N$ sedimentating spheres in fluid region Ω_{me}. Motion 2 consists of the motion of the same N sedimenting particles, two of which are shrunk to a smaller diameter $d'(<d)$ but which preserve the same buoyancy-corrected weights and centres of mass. The fluid occupies region $\mathscr{C}^{\mathrm{S}}_{\mathrm{UB}} = \Omega_{\mathrm{me}} \cup \mathscr{D}^{\mathrm{S}}_{\mathrm{UB}}$, where $\mathscr{D}^{\mathrm{S}}_{\mathrm{UB}} = \cup_{k=N-1}^{N} \Omega'_k$ is the region of fluid obtained by shrinking the spheres $k = N-1$ and $k = N$ (see Figure 7(b)); region Ω'_k is the spherical shell of inner diameter d' and outer diameter d obtained by shrinking sphere k. Lastly, motion 3 consists of motion 1 extended to the larger fluid domain $\mathscr{C}^{\mathrm{S}}_{\mathrm{UB}}$ of motion 2. We now characterize motions 2 and 3 in more detail; motion 1 is identical to motion 1 of Section 3.2.1.

The velocity field $\mathbf{u}^{(2)}$ of motion 2 satisfies the strong form (17)–(24) where the volume of particle k is given by

$$\mathscr{V}_k = \begin{cases} (\pi/6)d^3 & \text{if } k = 1, \ldots, N-2, \\ (\pi/6)d'^3 & \text{if } k = N-1, N \end{cases} \tag{53}$$

and the buoyancy-corrected weight of each particle is $\mathscr{W}$ such that, again, $\tau = N\mathscr{W}/\lambda^3$. As in our lower-bound proof, we have

$$\mathbf{u}^{(2)} = \arg \max_{\mathbf{w} \in B_{\mathscr{C}^{\mathrm{S}}_{\mathrm{UB}}}} J^{\mathrm{S}}_{\mathscr{C}^{\mathrm{S}}_{\mathrm{UB}}}(\mathbf{w}) \tag{54}$$

and thus define

$$\mathscr{U}^{(2)} = \frac{1}{N\mathscr{W}} J^{\mathrm{S}}_{\mathscr{C}^{\mathrm{S}}_{\mathrm{UB}}}(\mathbf{u}^{(2)}) \tag{55}$$

for the settling velocity.

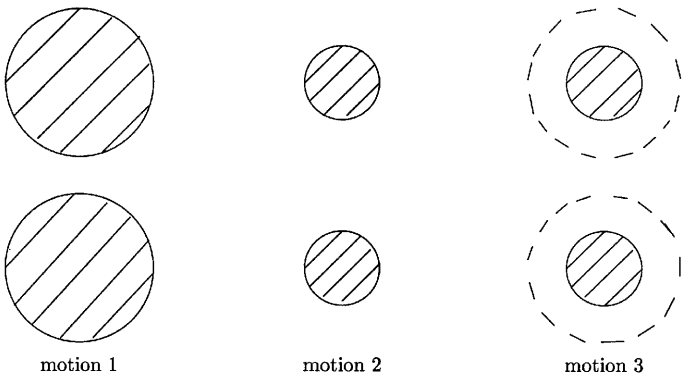

Figure 8. Motions for sedimentation upper-bound proof

Finally, motion 3 consists of motion 1 with region $\mathscr{D}^{\mathrm{S}}_{\mathrm{UB}}$ replaced by fluid. This motion is defined as

$$\mathbf{u}^{(3)} = \begin{cases} \mathbf{u}^{(1)} - D\mathbf{e}_1 - F\mathbf{e}_3 & \text{in } \mathscr{C}^{\mathrm{S}}_{\mathrm{UB}} \backslash \mathscr{D}^{\mathrm{S}}_{\mathrm{UB}}, \\ \mathbf{U}^{(1)}_k + \mathbf{R}^{(1)}_k \times (\mathbf{y} - \mathbf{y}_k) - D\mathbf{e}_1 - F\mathbf{e}_3 & \text{in } \Omega'_k,\ k = N-1, N, \end{cases} \tag{56}$$

where $\mathbf{U}^{(1)}_k$ and $\mathbf{R}^{(1)}_k$, $k = N-1, N$, are the translational and rotational velocities of the two unshrunk spheres of motion 1 and $D = (\mathscr{V}_{\Omega'}/\mathscr{V}_{\mathscr{C}^{\mathrm{S}}_{\mathrm{UB}}}) \sum_{k=N-1}^{N} (U^{(1)}_1)_k$ and $F = (\mathscr{V}_{\Omega'}/\mathscr{V}_{\mathscr{C}^{\mathrm{S}}_{\mathrm{UB}}}) \sum_{k=N-1}^{N} (U^{(1)}_3)_k$ are the shifts necessary to satisfy the horizontal homogeneity constraints of (31). Here $\mathscr{V}_{\Omega'}$ is the volume of the spherical shell of inner diameter d' and outer diameter d, and $\mathscr{V}_{\mathscr{C}^{\mathrm{S}}_{\mathrm{UB}}}$ is the volume of region $\mathscr{C}^{\mathrm{S}}_{\mathrm{UB}}$.

From equation (54) and the fact that $\mathbf{u}^{(3)} \in B_{\mathscr{C}^{\mathrm{S}}_{\mathrm{UB}}}$, it follows that

$$J^{\mathrm{S}}_{\mathscr{C}^{\mathrm{S}}_{\mathrm{UB}}}(\mathbf{u}^{(2)}) \geqslant J^{\mathrm{S}}_{\mathscr{C}^{\mathrm{S}}_{\mathrm{UB}}}(\mathbf{u}^{(3)}). \tag{57}$$

We then note that the velocity field of motion 3 produces the same value for the dissipation integral as the field of motion 1, since solid body rotation and translation of the fluid in region $\mathscr{D}^{\mathrm{S}}_{\mathrm{UB}}$ in motion 3 do not contribute to this integral. If we combine this observation with $I^{\mathrm{S}}_{\Omega_{\mathrm{me}}}(\mathbf{u}^{(1)}) = I^{\mathrm{S}}_{\mathscr{C}^{\mathrm{S}}_{\mathrm{UB}}}(\mathbf{u}^{(3)})$, it follows that

$$J^{\mathrm{S}}_{\Omega_{\mathrm{me}}}(\mathbf{u}^{(1)}) = J^{\mathrm{S}}_{\mathscr{C}^{\mathrm{S}}_{\mathrm{UB}}}(\mathbf{u}^{(3)}). \tag{58}$$

Finally, from (55), (57), (58) and (44) we get

$$\mathscr{U} = \mathscr{U}^{(1)} = \frac{1}{N\mathscr{W}} J^{\mathrm{S}}_{\Omega_{\mathrm{me}}}(\mathbf{u}^{(1)}) = \frac{1}{N\mathscr{W}} J^{\mathrm{S}}_{\mathscr{C}^{\mathrm{S}}_{\mathrm{UB}}}(\mathbf{u}^{(3)}) \leqslant \frac{1}{N\mathscr{W}} J^{\mathrm{S}}_{\mathscr{C}^{\mathrm{S}}_{\mathrm{UB}}}(\mathbf{u}^{(2)}) = \mathscr{U}^{(2)} \equiv \mathscr{U}_{\mathrm{UB}}, \tag{59}$$

which is the desired result. Note that (59) is a bound on the *dimensional* settling speed.

4. NUMERICAL METHODS

In this section we describe a finite element method for solving the 'microscale-prepared' porous media and sedimentation mesoscale problems. For notational simplicity we describe the formulation for a fluid domain Ω_{me}; however, identical procedures apply on the bounding domains $\mathscr{C}^{\mathrm{P}}_{\mathrm{LB}}$, $\mathscr{C}^{\mathrm{P}}_{\mathrm{UB}}$, $\mathscr{C}^{\mathrm{S}}_{\mathrm{LB}}$ and $\mathscr{C}^{\mathrm{S}}_{\mathrm{UB}}$. As a first step we mesh the mesocale fluid domain Ω_{me} by subdividing the geometry into conforming tetrahedra. We then descretize the variational weak forms of interest by using sub- and isoparametric Taylor–Hood elements[38] in which the pressure and velocity fields are approximated by linear and quadratic polynomials respectively.[39] Lastly, the resulting linear system of equations is solved by the Uzawa algorithm[40] and a nested conjugate gradient iteration scheme.[41]

This computational methodology is chosen for several reasons. First, unstructured tetrahedral meshes can readily adapt to the complex geometries of interest. Second, the finite element method is based on the variational formulation of the problems and thus readily accommodates both the microscale analyses and the complex (zero net force and torque) sedimentation natural boundary conditions. Third, iterative solution schemes require much less memory and fewer operations than direct solvers for the three-dimensional problems of interest.

4.1. Three-dimensional mesh generation

We subdivide the fluid region Ω_{me} into $\mathscr{K}$ conforming tetrahedra $\Omega^{k_{\mathrm{e}}}$ such that $\bar{\Omega}_{\mathrm{me},h} = \bigcup_{k_{\mathrm{e}}=1}^{\mathscr{K}} \bar{\Omega}^{k_{\mathrm{e}}}$, where $\Omega_{\mathrm{me},h}$ is the discretized fluid domain. Our mesh generation code is an adaptation of the mesh generation modules of FELISA, a three-dimensional compressible inviscid flow software package.[42] The FELISA mesh generator creates an unstructured, linear tetrahedral mesh for the specified geometry based on the advancing front technique; the user has control over the local mesh spacing h

through several different parameters and mechanisms. The nodes on the surface of the mesoscale cube are required to be periodic, consistent with the requisite periodic boundary conditions.

The meshes obtained from FELISA are linear, i.e. the tetrahedra have planar faces. In order to create a second-order subparametric mesh, we insert an additional node at the midpoint of each edge of each tetrahedron. To create an isoparameteric mesh from a subparametric mesh, we search for all the edges of the tetrahedra whose end-nodes are on a spherical particle and then move the corresponding mid-nodes to the particle surface. It has been found that this simple procedure can in some cases distort certain tetrahedra to the point that the Jacobian changes sign within those elements, thus losing coercivity (and preventing the subsequent conjugate gradient iteration from converging). This problem is avoided in one of two ways: by refining the mesh in the vicinity of a particle (which also helps resolve the flow field around the inclusion) or by first increasing the diameter of a sphere and then shrinking it to proper size after the mesh has been created, thereby radially stretching all tetrahedra on the sphere surface. More details on the mesh generation procedure are given in Reference 33. We remark that although our mesh generation procedure is automatic, additional geometric capabilities must be implemented to allow for dynamic simulation of suspensions, in which 'snapshots' are replaced by time-consistent evolution.

4.2. Porous media problem

4.2.1. Discretization. The discretization procedure follows three steps: non-dimensionalizing the variational weak form, restricting the spaces of admissible functions to the finite element spaces and representing the finite element spaces with appropriate bases to yield a linear algebraic system of equations.

We non-dimensionalize the variational weak form of the porous media problem (14), (15) by choosing d, $\Delta P d/L$ and $\Delta P d^2/\mu_{\text{co}} L$ for the length, pressure and velocity scales respectively, yielding the equations

$$a(\mathbf{u}, \mathbf{v}) - b(p, \mathbf{v}) = (\mathbf{f}, \mathbf{v}) \quad \forall \mathbf{v} \in (H^1_{0\#}(\Omega_{\text{me}}))^3, \tag{60}$$

$$-b(q, \mathbf{u}) = 0 \quad \forall q \in L^2_{\#,0}(\Omega_{\text{me}}), \tag{61}$$

where $\mathbf{u} \in (H^1_{0\#}(\Omega_{\text{me}}))^3$ and $p \in L^2_{\#,0}(\Omega_{\text{me}})$ are the non-dimensional velocity and pressure solutions respectively. Here

$$a(\mathbf{u}, \mathbf{v}) = \int_{\Omega_{\text{me}}} \frac{\partial u_i}{\partial y_j} \frac{\partial v_i}{\partial y_j} \, \mathrm{d}\mathbf{y}, \qquad b(p, \mathbf{v}) = \int_{\Omega_{\text{me}}} p \frac{\partial v_i}{\partial y_i} \, \mathrm{d}\mathbf{y}, \qquad (\mathbf{f}, \mathbf{v}) = \int_{\Omega_{\text{me}}} \delta_{1i} v_i \, \mathrm{d}\mathbf{y}.$$

We next construct a tetrahedral mesh consisting of $\mathscr{K}$ elements, N_{g}^{V} velocity nodes and N_{g}^{P} pressure nodes and introduce the (div-stable) Taylor–Hood finite element approximation spaces for the velocity field $\mathbf{u}_h$ and the pressure p_h: $Y_h^{\text{P}}(\Omega_{\text{me}}) = \{v|_{\Omega^{k_{\text{e}}}} \in \mathscr{P}_2(\Omega^{k_{\text{e}}})\} \cap H^1_{0\#}(\Omega_{\text{me}})$ and $W_h^{\text{P}}(\Omega_{\text{me}}) = \{q|_{\Omega^{k_{\text{e}}}} \in \mathscr{P}_1(\Omega^{k_{\text{e}}})\} \cap C_{\#,0}(\Omega_{\text{me}})$ respectively. Here $C_{\#,0}(\Omega_{\text{me}})$ is the space of continuous functions which are λ-periodic and have zero average and $\mathscr{P}_{\mathscr{N}_0}$ are the polynomials of total degree $\mathscr{N}_0$ defined over the tetrahedron $\Omega^{k_{\text{e}}}$. The discrete solutions $\mathbf{u}_h \in (Y_h^{\text{P}}(\Omega_{\text{me}}))^3$ and $p_h \in W_h^{\text{P}}(\Omega_{\text{me}})$ must then satisfy

$$a(\mathbf{u}_h, \mathbf{v}) - b(p_h, \mathbf{v}) = (\mathbf{f}, \mathbf{v}) \quad \forall \mathbf{v} \in (Y_h^{\text{P}}(\Omega_{\text{me}}))^3, \tag{62}$$

$$-b(q, \mathbf{u}_h) = 0 \quad \forall q \in W_h^{\text{P}}(\Omega_{\text{me}}). \tag{63}$$

We next represent our velocity and pressure approximations by the usual nodal bases and perform fifth-order Gaussian quadrature[33] of the elemental matrices to obtain the linear system

$$\underline{A}\underline{u}_{h_i} - \underline{D}_i^{\mathrm{T}} p_h = \underline{M}\underline{f}_i, \quad i = 1, 2, 3, \tag{64}$$

$$-\underline{D}_i \underline{u}_{h_i} = 0, \tag{65}$$

where $\underline{A}$ is the discrete (symmetric, positive definite) negative-Laplacian operator, $\underline{u}_{h_i} \in \mathscr{R}^{N_{\mathrm{g}}^{\mathrm{V}}}$ and $\underline{p}_h \in \mathscr{R}^{N_{\mathrm{g}}^{\mathrm{P}}}$ are respectively the (ith component of the) velocity and the pressure vectors of unknown global nodal values, $\underline{M}$ is the mass matrix, $\underline{D}_i$ is the discrete divergence operator and $\underline{f}_i = \delta_{1i}\underline{1}$ is the non-dimensional imposed pressure gradient. In addition to (64) and (65), we require for uniqueness that the pressure $\underline{p}_h$ have zero algebraic average.

Finally, the continuous permeability of (8) can be discretized in dimensionless form (scaled by d^2) as

$$\kappa_h^{\mathrm{P}} = \frac{1}{\lambda^3} \underline{1}^{\mathrm{T}} \underline{M} \underline{u}_{h_1}, \tag{66}$$

or equivalently,

$$\kappa_h^{\mathrm{P}} = \frac{1}{\lambda^3} \underline{u}_{h_i}^{\mathrm{T}} \underline{A} \underline{u}_{h_i}, \tag{67}$$

with summation over $i = 1, 2, 3$; here λ is non-dimensionalized by d. Equation (67) is obtained by multiplying (64) by $\underline{u}_{h_i}^{\mathrm{T}}$, summing over the repeated index i and recognizing that $\underline{u}_{h_i}^{\mathrm{T}} \underline{D}_i^{\mathrm{T}} = (\underline{D}_i \underline{u}_{h_i})^{\mathrm{T}} = 0$ from (65). We calculate κ_h^{P} in both ways to verify the code.

Given the exact dimensionless permeability κ (scaled by d^2), we define the discretization error as $E_h^{\mathrm{P}} \equiv |\kappa - \kappa_h^{\mathrm{P}}|$, which can be written as

$$E_h^{\mathrm{P}} \approx \frac{1}{\lambda^3} |a(\mathbf{u}, \mathbf{u}) - a(\mathbf{u}_h, \mathbf{u}_h)|. \tag{68}$$

The approximation sign reflects the fact that in (68) we ignore geometry approximations and quadrature errors, the former being particularly important in the subparametric case. We now select $\mathbf{v} = \mathbf{u}$ in (60) and $\mathbf{v} = \mathbf{u}_h$ in (62), use (61) and (63), subtract the resulting equations and take the absolute value to find

$$|a(\mathbf{u}, \mathbf{u}) - a(\mathbf{u}_h, \mathbf{u}_h)| = |(\mathbf{f}, (\mathbf{u} - \mathbf{u}_h))|. \tag{69}$$

Evoking the Cauchy–Schwartz inequality[41] to bound the right-hand side of (69) and using (68), we arrive at

$$E_h^{\mathrm{P}} \leqslant \frac{1}{\lambda^3} \|\mathbf{f}\|_{L^2} \|\mathbf{u} - \mathbf{u}_h\|_{L^2}, \tag{70}$$

where $\|\mathbf{v}\|_{L^2} = (\int_{\Omega_{\mathrm{me}}} \mathbf{v} \cdot \mathbf{v} \, \mathrm{d}\mathbf{y})^{1/2}$ is the L^2-norm over Ω_{me}. Equation (70) shows that the permeability error E_h^{P} is bounded by the finite element discretization error in the L^2-norm, which is $O(h^3)$ for second-order elements, where h is the mesh spacing.[43,44]

4.2.2. Iterative solution. In order to solve for the discrete velocity ($\underline{u}_{h_i}$) and pressure ($\underline{p}_h$) unknowns, we use the Uzawa saddle-decoupling algorithm. Recall that, to obtain the saddle decomposition, we multiply equation (64) by $\underline{D}_i\underline{A}^{-1}$ and evoke (65) to find

$$\underline{S}\underline{p}_h = -\underline{D}_i\underline{A}^{-1}\underline{M}\underline{f}_i, \tag{71}$$

$$\underline{A}\underline{u}_{h_i} = \underline{D}_i^{\mathrm{T}} p_h + \underline{M}\underline{f}_i, \quad i = 1, 2, 3, \tag{72}$$

where $\underline{S} \equiv \underline{D}_i\underline{A}^{-1}\underline{D}_i^{\mathrm{T}}$ (summation over repeated indices) is a symmetric, positive definite matrix. We first solve (71) for the pressure field based on nested conjugate gradient iteration. Once the pressure is determined, we then solve (72) for the velocity unknowns through three additional conjugate gradient iterations. Finally, we use either (66) or (67) to determine the permeability. Note that when the local mesh spacing h varies considerably within the mesoscale mesh, it is convenient and effective to precondition the outer pressure solver ($\underline{S}$) with the diagonal lumped pressure mass matrix.[40,41] Although we have presented the discrete system in terms of *global* matrices, we operate in practice with *local* data structures.[33]

4.3. Sedimentation problem

4.3.1. Discretization. Similarly to the porous media problem, we arrive at the discrete system of equations by non-dimensionalizing the variational weak form, restricting the velocity and pressure spaces, representing the velocity and pressure with the usual bases and performing quadrature.

Non-dimensionalizing the variational weak form (33)–(35) for the case of monodisperse spheres by choosing d, $(\rho_{\mathrm{di}} - \rho_{\mathrm{co}})gd$ and $(\rho_{\mathrm{di}} - \rho_{\mathrm{co}})gd^2/\mu_{\mathrm{co}} = 6\mathscr{W}/\pi\mu_{\mathrm{co}}d$ for the length, pressure and velocity scales respectively yields

$$a'(\mathbf{u}, \mathbf{v}) - b(p', \mathbf{v}) = c(\mathbf{f}, \mathbf{v}) - (1 - c)l(\mathbf{v}) \quad \forall \mathbf{v} \in Y(\Omega_{\mathrm{me}}), \tag{73}$$

$$-b(q, \mathbf{u}) = 0 \quad \forall q \in L^2_{\#,0}(\Omega_{\mathrm{me}}), \tag{74}$$

$$-\eta[(\mathbf{f}, \mathbf{u}) + l(\mathbf{u})] = 0 \quad \forall \eta \in \mathscr{R}, \tag{75}$$

where $c = N_{\mathrm{p}}\pi d^3/6\lambda^3$ is the sphere volume concentration, $\mathbf{u} \in Y(\Omega_{\mathrm{me}})$ and $p' \in L^2_{\#,0}(\Omega_{\mathrm{me}})$ are the (non-dimensional) velocity and pressure solutions respectively and Y is the functional space defined in (31). Here

$$a'(\mathbf{u}, \mathbf{v}) = \int_{\Omega_{\mathrm{me}}} \frac{\partial v_i}{\partial y_j}\left(\frac{\partial u_i}{\partial y_j} + \frac{\partial u_j}{\partial y_i}\right) \mathrm{d}\mathbf{y}, \qquad (\mathbf{f}, \mathbf{v}) = \int_{\Omega_{\mathrm{me}}} \delta_{2i} v_i \, \mathrm{d}\mathbf{y}, \qquad l(\mathbf{v}) = \frac{\pi}{6}\sum_{k=1}^{N_{\mathrm{p}}} (V_2)_k,$$

where $(V_2)_k$ is such that $\mathbf{v}|_{\partial\Omega_k} = \mathbf{V}_k + \mathbf{P}_k \times (\mathbf{y} - \mathbf{y}_k)$, $k = 1, \ldots, N_{\mathrm{p}}$.

As for the porous media problem, we introduce a tetrahedral mesh consisting of k elements and our two discrete spaces $Y_h^{\mathrm{S}}(\Omega_{\mathrm{me}}) = \{(v_1, v_2, v_3)|_{\Omega^{k_{\mathrm{e}}}} \in (\mathscr{P}_2(\Omega^{k_{\mathrm{e}}}))^3\} \cap Y(\Omega_{\mathrm{me}})$ and $W_h^{\mathrm{S}}(\Omega_{\mathrm{me}}) = \{q|_{\Omega^{k_e}} \in \mathscr{P}_1(\Omega^{k_{\mathrm{e}}})\} \cap C_{\#,0}(\Omega_{\mathrm{me}})$. The discrete solutions $\mathbf{u}_h \in Y_h^{\mathrm{S}}(\Omega_{\mathrm{me}})$ and $p'_h \in W_h^{\mathrm{S}}(\Omega_{\mathrm{me}})$ must then satisfy

$$a'(\mathbf{u}_h, \mathbf{v}) - b(p'_h, \mathbf{v}) = c(\mathbf{f}, \mathbf{v}) - (1 - c)l(\mathbf{v}) \quad \forall \mathbf{v} \in Y_h^{\mathrm{S}}(\Omega_{\mathrm{me}}), \tag{76}$$

$$-b(q, \mathbf{u}_h) = 0 \quad \forall q \in W_h^{\mathrm{S}}(\Omega_{\mathrm{me}}), \tag{77}$$

$$-\eta[(\mathbf{f}, \mathbf{u}_h) + l(\mathbf{u}_h)] = 0 \quad \forall \eta \in \mathscr{R}. \tag{78}$$

Note that condition (78), originating in (22), sets the level of u_{h_2}.

Turning now to the representation of our unknowns, we note that the velocity field, as well as all variations $\mathbf{v} \in Y_h^{\mathrm{S}}(\Omega_{\mathrm{me}})$, must be consistent with solid body motion of the particles. In order to make

the standard nodal (finite element) representation of the bases conform with this essential kinematic requirement, we construct a mapping matrix $\underline{Q}$:[33,45]

$$\underline{u}_h = \underline{Q}\underline{u}_h^{\text{master}}, \tag{79}$$

in which $\underline{u}_h \in \mathscr{R}^{3N_g^V}$ and $\underline{u}_h^{\text{master}} \in \mathscr{R}^{3N_{\text{dof}}}$. Here $3N_g^V$ is the total number of velocity degrees of freedom in the absence of any boundary conditions and $3N_{\text{dof}}$ is the number of actual velocity degrees of freedom, where $N_{\text{dof}} = N_g^V - N_{\text{surf}} + 2N_p$ and N_{surf} is the number of velocity nodes on all particles. Note that in the sedimentation formulation we *concatenate* all three velocity components into one vector, $\underline{u}_h^T = (\underline{u}_{h_1}^T \ \underline{u}_{h_2}^T \ \underline{u}_{h_3}^T)$, since the bilinear form $a'(\cdot,\cdot)$ couples the three directions. In effect, the matrix $(\underline{Q})$ maps the master degrees of freedom of the system $(3N_{\text{dof}})$ onto the finite element slave degrees of freedom $(3N_g^V)$ created by the mesh generator.

We now show an example of how $\underline{Q}$ maps the six degrees of freedom of particle k onto the N_s surface nodal values of the particle in the (say) $i = 1$ direction. For this subset of nodes, equation (79) reads

$$\begin{pmatrix} u_{h_1}^1 \\ \vdots \\ u_{h_1}^n \\ \vdots \\ u_{h_1}^{N_s} \end{pmatrix} = \begin{pmatrix} 1 & 0 & 0 & 0 & ((y_3^1)_k - (y_3)_k) & -((y_2^1)_k - (y_2)_k) \\ \vdots & & & & & \\ 1 & 0 & 0 & 0 & ((y_3^n)_k - (y_3)_k) & -((y_2^n)_k - (y_2)_k) \\ \vdots & & & & & \\ 1 & 0 & 0 & 0 & ((y_3^{N_s})_k - (y_3)_k) & -((y_2^{N_s})_k - (y_2)_k) \end{pmatrix} \begin{pmatrix} (U_1)_k \\ (U_2)_k \\ (U_3)_k \\ (R_1)_k \\ (R_2)_k \\ (R_3)_k \end{pmatrix}, \tag{80}$$

where $(y_i^n)_k$ and $(y_i)_k$, $i = 1, 2, 3$, are the co-ordinates of the nth surface node and the centre of mass of particle k respectively and $u_{h_1}^n$ is the value of the velocity vector at node n in the $i = 1$ direction. Of course, $\underline{Q}$ operates as an identity on those entries of $\underline{u}_h^{\text{master}}$ that correspond to degrees of freedom that are not on a particle.

The great convenience of the '$\underline{Q}$' mapping is that we can now write our discrete equations in terms of standard bases on a standard mesh and standard elemental matrices. Our linear system becomes

$$\underline{Q}^T\underline{A}'\underline{Q}\underline{u}_h^{\text{master}} - \underline{Q}^T\underline{D}'^T\underline{p}_h' = \underline{Q}^T c\underline{M}'\underline{1}' - (1-c)\underline{L}^{\text{master}}, \tag{81}$$

$$-\underline{D}'\underline{Q}\underline{u}_h^{\text{master}} = 0, \tag{82}$$

$$\underline{1}'^T\underline{M}'\underline{Q}\underline{u}_h^{\text{master}} + \frac{\pi}{6}\sum_{k=1}^{N_p}(U_2)_k = 0, \tag{83}$$

where $\underline{A}'$ is the 'stress formulation' of the discrete Laplacian that couples all three velocity directions, $\underline{D}' = (\underline{D}_1 \ \underline{D}_2 \ \underline{D}_3)$ with the $\underline{D}_i$ as defined in Section 4.2.1, $\underline{M}'$ is the block-diagonal matrix formed by the component mass matrices $\underline{M}$, and $\underline{1}'$ is the $3N_g^V$-vector which is unity only for the degrees of freedom associated with the second vector component of the velocity. Finally, the vector $(\underline{L}^{\text{master}})^T = (\underline{L}_1^T \ \underline{L}_2^T \ \underline{L}_3^T)$ is, on a global level, given by

$$(L_i)_j = \begin{cases} \delta_{2i}\pi/6 & \text{if } j \text{ is a } \textit{translational} \text{ degree of freedom of sphere } k, \\ 0 & \text{otherwise,} \end{cases} \tag{84}$$

where $i = 1, 2, 3$, and $j = 1, \ldots, N_{\text{dof}}$. Note that the right-hand side of (81) is obtained in three steps: first, we calculate $c\underline{M}'\underline{1}'$ on the slave degrees of freedom; second, we map the slave degrees of freedom onto the master degrees of freedom via $\underline{Q}^T$ (i.e. perform $\underline{Q}^T c\underline{M}'\underline{1}'$); finally, we subtract $(1-c)\underline{L}^{\text{master}}$ to obtain the right-hand-side forcing term.

4.3.2. Iterative solution. The solution of (81)–(83) is obtained using the Uzawa algorithm described in the previous section. For the sedimentation problem the saddle decomposition takes the form

$$\underline{S}\underline{p}'_h = -\underline{D}'\underline{Q}(\underline{Q}^{\mathrm{T}}\underline{A}'\underline{Q})^{-1}[\underline{Q}^{\mathrm{T}}c\underline{M}'\underline{1}' - (1-c)\underline{L}^{\mathrm{master}}], \tag{85}$$

$$(\underline{Q}^{\mathrm{T}}\underline{A}'\underline{Q})\underline{u}_h^{\mathrm{master}} = \underline{Q}^{\mathrm{T}}(\underline{D}'^{\mathrm{T}}\underline{p}'_h + c\underline{M}'\underline{1}') - (1-c)\underline{L}^{\mathrm{master}}, \tag{86}$$

where $\underline{S} = \underline{D}'\underline{Q}(\underline{Q}^{\mathrm{T}}\underline{A}'\underline{Q})^{-1}\underline{Q}^{\mathrm{T}}\underline{D}'^{\mathrm{T}}$. Note that both $\underline{Q}^{\mathrm{T}}\underline{A}'\underline{Q}$ and $\underline{S}$ are positive definite (or positive semidefinite) matrices. The pressure preconditioner described in Section 4.2.2 is again used to accelerate the outer iteration associated with (85).

Equation (83) is implemented similarly to the uniqueness conditions on the velocity components, (23), and on the pressure, (24). For example, (83) is satisfied by first calculating the (non-zero) value of the left-hand side with the velocity results of a given iteration and then subtracting this result, divided by the volume of the mesoscale cube, from the velocity vector in the $i = 2$ direction. In infinite precision arithmetic, (83) need only be satisfied after the solver that inverts $\underline{Q}^{\mathrm{T}}\underline{A}'\underline{Q}$ has converged; however, to ensure that the conjugate gradient iteration converges in finite precision arithmetic, we satisfy condition (83) every, say, 100 iterations. Note also that when integrating over the fluid region Ω_{me}, the discrete volume $\mathscr{V}_{\mathrm{me},h}$ of the sub- or isoparametric domain $\Omega_{\mathrm{me},h}$ will differ slightly from the exact value $\mathscr{V}_{\mathrm{me}}$. In the continuous formulation the solvability of the variational weak form (33)–(35) is guaranteed by the correct choice of the backflow pressure gradient $\tau = N_{\mathrm{p}}\mathscr{W}/\lambda^3$ (see Section 2.2). In the discrete formulation, solvability is guaranteed by a discrete backflow pressure gradient

$$\tau_h = \frac{N_{\mathrm{p}}\mathscr{W}}{\sum_{k=1}^{N_{\mathrm{p}}}\mathscr{V}_k + \mathscr{V}_{\mathrm{me},h}};$$

non-dimensionally, τ_h is equivalent to the discrete volume fraction

$$c_h = \frac{\sum_{k=1}^{N_{\mathrm{p}}}\mathscr{V}_k}{\sum_{k=1}^{N_{\mathrm{p}}}\mathscr{V}_k + \mathscr{V}_{\mathrm{me},h}}.$$

It follows that we must replace the volume fraction c with c_h in (85) and (86).

5. RESULTS AND CONCLUSIONS

In this section we present and discuss our results and offer some conclusions. In Section 5.1 we present the porous media results for a simple cubic array of spheres and validate the results against semi-analytical solutions. Subsequently, we implement the microscale treatment of Section 3.1 to reach maximum packing density and briefly discuss low-Reynolds-number fluidization. In Section 5.2 the sedimentation methodology is validated by relating the porous media results to the settling velocity of a simple cubic array of spheres. We then look at two spheres settling in a mesoscale cell, both with and without our microscale treatment, and compare these results with those obtained for a pair of spheres settling in an infinite fluid. Finally, the qualitative behaviour of three spheres in the mesoscale cell is briefly discussed.

Note that all numerical results presented in this section are dimensionless: the permeability is non-dimensionalized with respect to the square of the sphere diameter d, the settling speed is non-dimensionalized by $(\rho_{\mathrm{di}} - \rho_{\mathrm{co}})gd^2/\mu_{\mathrm{co}} = 6\mathscr{W}/\pi\mu_{\mathrm{co}}d$ and, as before, all linear dimensions that appear

in the variational weak forms are non-dimensionalized with respect to d. However, for discussion purposes, mesoscale lengths are in reference to a unit edge ($\lambda = 1$). Dimensional variables, when needed, will be marked by a 'hat' (e.g. $\hat{\mathbf{u}}$, $\hat{\kappa}$).

5.1. Porous media results

5.1.1. Numerical results. Exact results for creeping flow through a simple cubic array of spheres are presented in Reference 17 in the form of a concentration-dependent drag coefficient K defined as

$$K \equiv \hat{D}/\hat{D}_{\text{Stokes}}, \tag{87}$$

where $\hat{D}_{\text{Stokes}}$ is the Stokes drag on a single sphere moving at a constant speed $\hat{U}_\infty$ in an unbounded fluid and $\hat{D}$ is the drag on a sphere in the simple cubic array moving at the same speed $\hat{U}_\infty$ in a quiescent fluid. The drag coefficient can be related to the permeability quite simply. First, a momentum balance on the mesoscale cell tells us that the pressure force induced by the macroscopic pressure gradient $(\Delta\hat{P}/\hat{L})$ balances the drag force $\hat{D}$; second, through Darcy's law, $\hat{U}_\infty = -(\hat{\kappa}/\mu_{\text{co}})\Delta\hat{P}/\hat{L}$, we can then relate the drag to the dimensionless permeability as

$$\kappa = 1/18cK. \tag{88}$$

Table I compares our permeability results with those of Reference 17 for different sphere concentrations; the agreement is very good.

To ensure that our code behaves correctly, we observe how the error decreases as the mesh is refined for a given sphere concentration $c = \pi d^3/6\lambda^3$. In particular, we plot in Figure 9, in log–log format, the error E_h^{P} versus the nominal mesh spacing h for a concentration $c = 0{\cdot}125$, where $E_h^{\text{P}} \equiv |\kappa - \kappa_h^{\text{P}}|$. Here κ is the exact permeability and κ_h^{P} is the finite element discrete permeability. The data of Figure 9 are obtained by using subparametric and isoparametric $\mathscr{P}_2$–$\mathscr{P}_1$ (Taylor–Hood) tetrahedral elements with a nominal mesh spacing h that varies from 0·17 to 0·07 in a cube of unit side (corresponding to about 3,000–25,000 degrees of freedom for each velocity component). The calculations are performed on a high end HP 9000 workstation and require from several minutes to several hours of CPU time. From the simple theory of Section 4.2.1 we expect, based on (70), $O(h^3)$ convergence. Figure 9 confirms that the convergence rate is indeed third-order for isoparametric elements; for subparametric elements we obtain only $O(h^2)$ convergence owing to the skin error associated with the surface mesh of the sphere. On an absolute scale the isoparametric error is much smaller than the subparametric error, the former clearly being the more efficient approach.

In order to achieve maximum packing density ($c = 0{\cdot}5236$), we *must* implement the microscale treatment described in Section 3.1, since a mesh cannot be generated when the sphere touches the

Table I. Permeability versus concentration results for simple cubic array of spheres

Concentration	$\kappa_{\text{Ref. 17}}$	κ_h^{P}
0·008	4.554	4·507
0·064	0·3089	0·3080
0·125	0·1036	0·1031
0·216	0·03456	0·03455
0·343	0·01052	0·01047
0·45	0·004394	0·004374

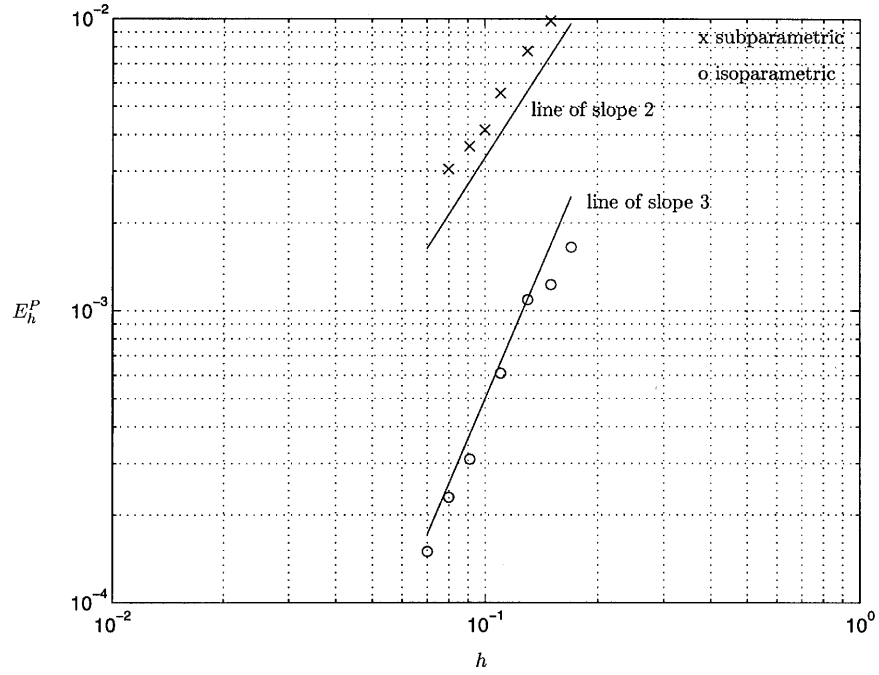

Figure 9. Convergence plot for permeability formulation: error E_h^{P} versus nominal mesh spacing h for simple cubic array at concentration $c = 0{\cdot}125$

sides of the mesoscale cell, i.e. comes into contact with spheres from neighbouring cells. Following the procedures of Section 3.1, we obtain the results shown in Table II, in which we see that the microscale treatment allows us to bound the permeability rather sharply. As expected, as the nip region increases in size (i.e. as the nip cylinder diameter increases), the bounds become cruder and the computational problem, having fewer degrees of freedom, becomes easier. Figure 10 depicts part of a mesh for the lower-bound geometry. The use of the bounding procedures is crucial in analysing random porous media, especially at medium to high concentrations when particles in close proximity are the norm and not the exception.

5.1.2. Physical results. As described in the previous subsection, we successfully reproduce the well-known results for permeability in simple cubic arrays. Although this geometry is seldom a good model for the spatial distribution of particles in real porous media, it can still lead to reasonable quantitative estimates. For instance, we can relate the permeability of a packed bed to the concept of

Table II. Permeability bounds for maximum packing density $c = 0{\cdot}5236$ for simple cubic array. The nip diameter is the diameter of the cylindrical region that is added to or subtracted from the fluid domain, relative to the side of the mesoscale cube, λ

Nip Diameter	$\kappa^{\mathrm{P}}_{h,\mathrm{LB}}$	$\kappa_{\mathrm{Ref.\,17}}$	$\kappa^{\mathrm{P}}_{h,\mathrm{UB}}$
0·2	0·002459	0·002520	0·002588
0·25	0·002250	0·002520	0·002862

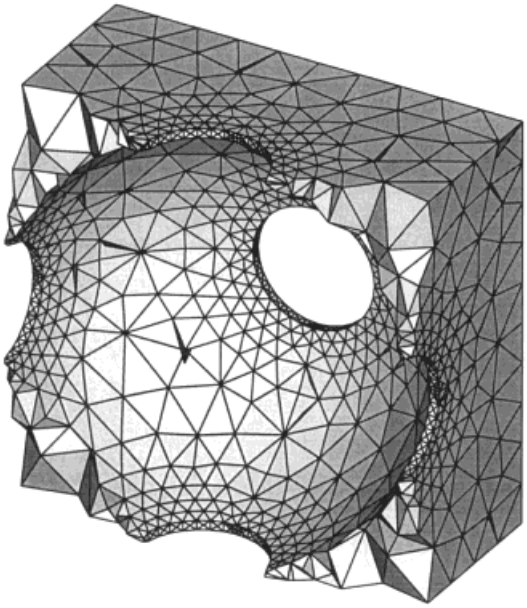

Figure 10. Mesh cross-section for permeability lower-bound geometry for maximum packing density ($c = 0{\cdot}5236$) for simple cubic array

minimum fluidization velocity,[46] $U_{\mathrm{mf}} = (1/\lambda^3) \int_{\Omega_{\mathrm{me}}} (u_1)_{\mathrm{mf}}\, \mathbf{dy}$, which is the average fluid velocity that creates a pressure drop across a packed bed of particles such that the pressure drop balances the buoyancy-corrected weight of the particles; it is typically expected that a velocity greater than U_{mf} leads to fluidization. Using Darcy's law, we can write the pressure drop in terms of the minimum fluidization velocity, the fluid viscosity and the permeability, obtaining

$$Re_{\mathrm{mf}} = \kappa c(GaMv), \tag{89}$$

where $Re_{\mathrm{mf}} = \rho_{\mathrm{co}} U_{\mathrm{mf}} d/\mu_{\mathrm{co}}$ is the fluidization Reynolds number, $Ga = d^3 g \rho_{\mathrm{co}}^2/\mu_{\mathrm{co}}^2$ is Galileo's number and $Mv = (\rho_{\mathrm{di}} - \rho_{\mathrm{co}})/\rho_{\mathrm{co}}$. Based on our results for simple cubic arrays of spheres, (89) becomes

$$Re_{\mathrm{mf}} = 1{\cdot}32 \times 10^{-3}(GaMv), \tag{90}$$

where $\kappa c = 1{\cdot}32 \times 10^{-3}$ is obtained by setting $c = 0{\cdot}5236$ and $\kappa = \kappa_h^{\mathrm{p}} = 0{\cdot}002524$; the latter is the arithmetic mean of the sharpest bounds of Table II.

Empirical correlations that relate Re_{mf}, Ga and Mv are abundant in the literature.[46] Unfortunately, most of the formulae are not linear in $GaMv$, since they account for flow regimes that range from low to intermediate Reynolds numbers. However, among those formulae that are linear, we find that the empirical coefficient κc varies from 8×10^{-4} to 8×10^{-3} for different types of randomly packed beds, which demonstrates that our regular array estimate is of the correct order of magnitude. The empirical coefficient is most probably a strong function of the spatial distribution of the particles.

5.2. Sedimentation results

5.2.1. Numerical results. We begin by analysing the sedimentation of a simple cubic array of spheres and compare these results with those for porous media, since for this geometry the two problems yield easily interchangeable effective properties. Both flows are caused by a pressure

gradient: in porous media flow the pressure gradient is externally imposed, whereas in sedimentation the pressure gradient is created by the buoyancy-corrected weight of the particles (i.e. the backflow pressure gradient). Relating the settling speed of a simple cubic array to the corresponding permeability is thus fairly simple. First, we adopt a co-ordinate system that is fixed on a sedimenting sphere and recognize that

$$\hat{u}_{1,\text{permea}} = \hat{u}_{2,\text{sed}} - \hat{U}_2, \tag{91}$$

where $\hat{u}_{1,\text{permea}}$ and $\hat{u}_{2,\text{sed}}$ are the *dimensional* velocity fields in the direction of the pressure gradients for the permeability and sedimentation flows respectively and $\hat{U}_2$ is the *dimensional* co-ordinate system shift (i.e. the vertical velocity of a settling sphere). Second, we use Darcy's law, $\langle \hat{u}_{1,\text{permea}} \rangle_v = -(\hat{\kappa}/\mu_{\text{co}})\Delta P/L$, where $\langle \hat{u}_{1,\text{permea}} \rangle_v = -\hat{U}_2$ from (91) and the zero-net-volume-flow-rate condition (22), and $-\Delta P/L = \tau = \mathscr{W}/\lambda^3$. Non-dimensionalizing all quantities as in Section 4.3.1, it follows that

$$\kappa = -U_2/c = \mathscr{U}/c \tag{92}$$

for simple cubic arrays, where all quantities in (92) are dimensionless.

Figure 11 is a plot of $E_h^{\text{S}} \equiv |\kappa - \kappa_h^{\text{S}}|$ versus h for a concentration $c = 0{\cdot}125$ for isoparametric $\mathscr{P}_2 - \mathscr{P}_1$ elements, where $\kappa_h^{\text{S}} = \mathscr{U}_h/c$, i.e. the sedimentation calculation prediction for the permeability. The mesh spacing ranges from $h = 0{\cdot}15$ to $0{\cdot}091$ in a mesoscale cell of unit side; the corresponding CPU times range from 1 to 12 h. The data points seem to suggest third-order convergence, as expected. Table III presents the sedimentation results with greater precision. When compared with the porous media results of Table I, it is clear that the porous media and sedimentation predictions for the permeability are close but do not coincide. This is because, although the formulations are equivalent in the continuous sense, they are not equivalent in the discrete sense. In particular, in the porous media formulation we force the velocity to be zero on the sphere boundary, whereas in the sedimentation formulation we require force and torque balances on the sphere. Figure 12 is a summary of our permeability results for both formulations; note that we have included the porous media maximum packing density result as a vertical 'error bar' that represents the crudest of the bounds of Table II.

Next, we consider a *pair* of particles in the mesoscale cell. In particular, we analyse a mesoscale cell with edges of unit length containing two spheres of diameter $d = 0{\cdot}1$ separated by an intercentre distance $l_{\text{c}} = 0{\cdot}2$. We consider three cases corresponding to three orientations of the line connecting the centres of the spheres; in all three cases the centres of the spheres lie on the $y_3 = 0{\cdot}5$ plane. Figure 13(a) shows the surface mesh for case 1, which corresponds to the line of centres being perpendicular to the gravity vector. In case 2 the line of centres is parallel to gravity, as shown in Figure 13(b). Finally, Figure 13(c) shows case 3, in which the line of centres makes an angle of $\pi/4$ with the horizontal. Table IV summarizes for each of three cases the translational and rotational degrees of freedom of each particle obtained on meshes with about 7,000 elements and 10,000 degrees of freedom for each velocity component. Note that we have tried various sphere arrangements such that the pair is at a non-zero angle with the $y_3 = 0{\cdot}5$ plane and found that our results remain largely invariant.

Although the three cases discussed do not *require* the microscale treatment of Section 3.2, they are a convenient vehicle by which to illustrate the bounds. For each of the original cases we introduce the lower- and upper-bound analyses of Section 3.2. The lower bound is obtained by connecting the pair of spheres with a cylinder of diameter $d_{\text{c}} = 0{\cdot}08$ and merging the two spheres into a single particle, a dumb-bell; the upper bound is obtained by shrinking both spheres to a diameter $d' = 0{\cdot}08$. Table V summarizes the dumb-bell motions and Table VI summarizes the motions of the two spheres of diameter d'.

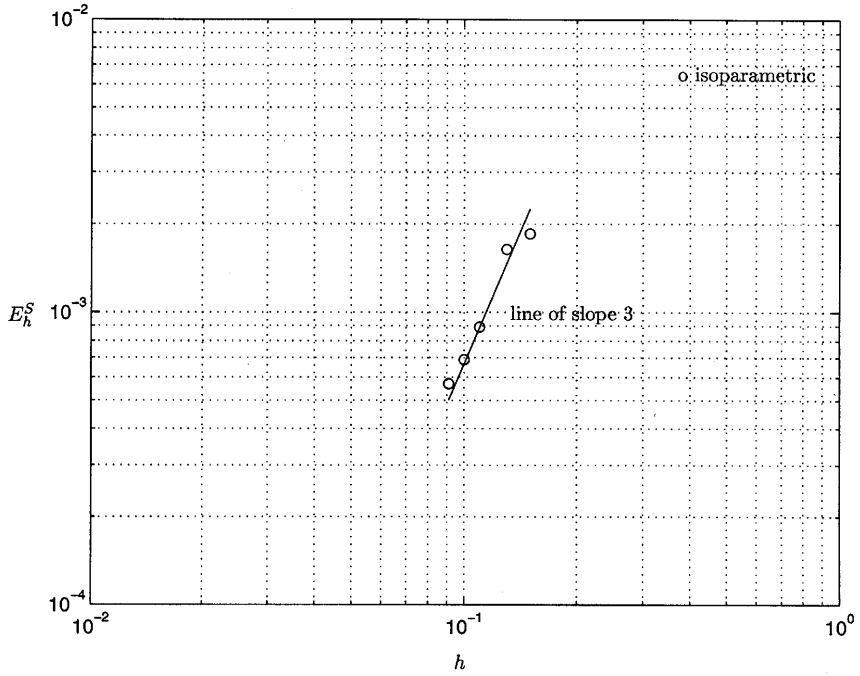

Figure 11. Convergence plot for sedimentation formulation: error E_h^{S} versus nominal mesh spacing h for simple cubic array at concentration $c = 0{\cdot}125$

Finally, we show the bounds for the settling speeds in Table VII. As mentioned above, the three cases analysed are not geometrically stiff and thus implementing the bounding procedures does not decrease the number of degrees of freedom significantly; the bounds are nevertheless quite sharp, as the fluid prefers to flow around the intersphere gap. Note that (59) is a dimensional result, $\hat{\mathscr{U}} \leqslant \hat{\mathscr{U}}_{\mathrm{UB}}$. In Tables IV and VI the velocities are scaled by $6\mathscr{W}/\pi\mu_{\mathrm{co}}d$ and $6\mathscr{W}/\pi\mu_{\mathrm{co}}d'$ respectively and thus (59) implies that

$$\mathscr{U} \leqslant \frac{d}{d'}\mathscr{U}_{\mathrm{UB}} \equiv \bar{\mathscr{U}}_{\mathrm{UB}}. \tag{93}$$

It is thus $\bar{\mathscr{U}}_{\mathrm{UB}}$ and not $\mathscr{U}_{\mathrm{UB}}$ that we present in Table VII and it is seen that (93) is indeed satisfied.

Table III. Sedimentation results: sedimentation calculation prediction for permeability versus concentration for simple cubic array of spheres

Concentration	κ_h^{S}
0·008	4·468
0·064	0·3068
0·125	0·1028
0·216	0·03432
0·343	0·01046
0·45	0·004368

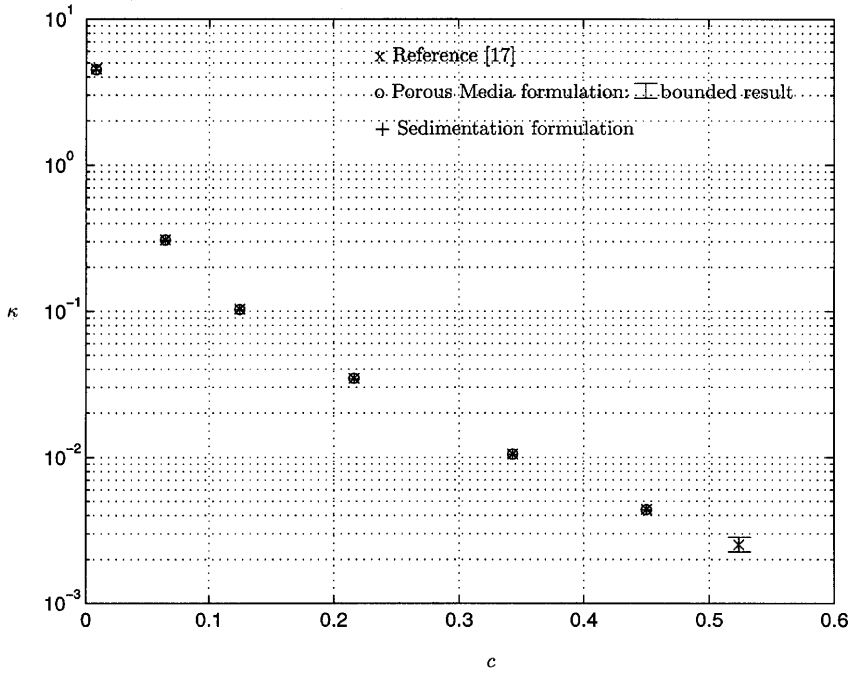

Figure 12. Permeability κ versus concentration c for simple cubic array of spheres

5.2.2. Physical results. We briefly discuss several physical aspects of the flows presented in the previous subsection, beginning with the simple cubic array. One interesting aspect of this well-known flow is that the settling velocity of the array is always smaller than the settling velocity of a single sphere in an unbounded medium, $\mathscr{U}_{\text{Stokes}} = 1/18 = 0{\cdot}05556$ (in non-dimensional form). We observe that for the smallest concentration we reach, $c = 0{\cdot}000268$, the settling speed is $\mathscr{U}_h = 0{\cdot}04867$, which is less than but close to $\mathscr{U}_{\text{Stokes}}$. The lowest settling speed is achieved at the maximum concentration $c = 0.5236$; in this close-packed limit the settling speed is $\mathscr{U}_h = \kappa_h^{\text{P}} c = 1{\cdot}32 \times 10^{-3}$, which is much less than $\mathscr{U}_{\text{Stokes}}$. This phenomenon, known as hindered settling, is common to all sedimentation processes that occur in any kind of impermeable 'backflow' container: the upward flow of fluid retards the motion of the suspension, so N_{p} particles in a mesoscale cell fall slower than the same N_{p} particles in an unbounded medium. Note that sedimentation in *unbounded* fluids has a peculiar behaviour: since each additional particle drags along with it some fluid and therefore other particles, an infinite number of particles falls at an infinite speed.[47]

The hindered settling argument also applies to the pair of spheres discussed in the previous subsection. Happel and Brenner[47] obtain analytical results for two spheres falling in an unbounded fluid based on the method of reflections. For example, when the sphere centres are separated by a distance that is three times their radius, the analytical study predicts the settling speed $\mathscr{U}_{\text{HB,hor}} = 0{\cdot}07059$ when the line of centres is horizontal and $\mathscr{U}_{\text{HB,ver}} = 0{\cdot}07959$ when the line of centres is in the direction of gravity. For spheres of diameter $d = 0{\cdot}2$ and interparticle distance $l_{\text{c}} = 0{\cdot}3$ in a mesoscale cube of unit edge we calculate $\mathscr{U}_{\text{h,hor}} = 0{\cdot}03956 < \mathscr{U}_{\text{HB,hor}}$ and $\mathscr{U}_{\text{h,ver}} = 0{\cdot}05063 < \mathscr{U}_{\text{HB,ver}}$, consistent with the hindered settling theory. Again, in the limit of zero concentrations ($c \to 0$) the settling rates should coincide.

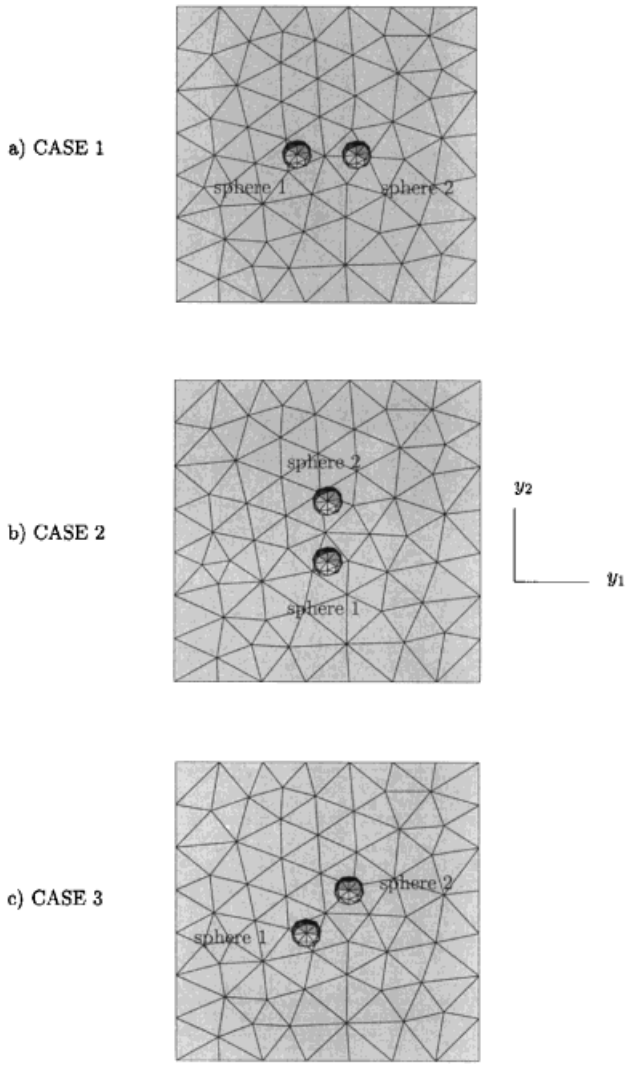

Figure 13. Sedimentation of two spheres in a mesoscale cell: surface meshes of spheres and one face of mesoscale cell

Table IV. Translational and rotational degrees of freedom of two spheres ($k = 1, 2$) falling in a mesoscale cube for the three cases described in the text and depicted in Figure 13

Case	k	$(U_1)_k$	$(U_2)_k$	$(U_3)_k$	$(R_1)_k$	$(R_2)_k$	$(R_3)_k$
1	1	—	−0·050322	—	—	—	−0·007421
1	2	—	−0·050324	—	—	—	0·007412
2	1	—	−0·059150	—	—	—	—
2	2	—	−0·059184	—	—	—	—
3	1	−0·003920	−0·054733	—	—	—	−0·005346
3	2	−0·003917	−0·054708	—	—	—	0·005288

Table V. Translational and rotational degrees of freedom of a dumb-bell in a mesoscale cube (lower-bound geometry) for the three cases described in the text and depicted in Figure 13

Case	(U_1)	(U_2)	(U_3)	(R_1)	(R_2)	(R_3)
1	—	−0·047004	—	—	—	—
2	—	−0·058298	—	—	—	—
3	−0·005217	−0·052605	—	—	—	—

Table VI. Translational and rotational degrees of freedom of two shrunk spheres in a mesoscale cube (upper-bound geometry) for the three cases described in the text and depicted in Figure 13

Case	k	$(U_1)_k$	$(U_2)_k$	$(U_3)_k$	$(R_1)_k$	$(R_2)_k$	$(R_3)_k$
1	1	—	−0·050980	—	—	—	−0·004649
1	2	—	−0·050981	—	—	—	0·004752
2	1	—	−0·058560	—	—	—	—
2	2	—	−0·05865	—	—	—	—
3	1	−0·003441	−0·054772	—	—	—	−0·003367
3	2	−0·003456	−0·054749	—	—	—	0·003316

Table VII. Bound results on settling speed of two spheres in a mesoscale cube for the three cases described in the text and depicted in Figure 13

Case	$\mathscr{U}_{h,\mathrm{LB}}$	$\mathscr{U}_h$	$\bar{\mathscr{U}}_{h,\mathrm{UB}}$
1	0·04700	0·05032	0·06372
2	0·05830	0·05916	0·07328
3	0·05261	0·05472	0·06845

There are also some interesting qualitative features associated with the fall of two spheres in a periodic cell. For example, the interparticle distance l_c remains constant throughout the fall. This can be explained through the concept of kinematic reversability of Stokes flows:[48,49] by reversing the flow and the boundary motions as well as the pressure gradient and body forces, we are presented with a new flow that still satisfies the equations of motion. For the case of two spheres with their line of centres parallel to gravity it is not intuitive that the distance l_c should remain constant; however, this must be the case. To show this, assume that, for example, the spheres diverged from each other; but, by reversing the flow—equivalent to changing the sign of the gravity vector—the spheres would reverse their motions. This is clearly incorrect, since rotating the gravity vector by π should yield the same flow—diverging spheres cannot become converging. Thus the spheres must fall at constant separation. The same argument can be made for a pair of spheres oriented in any way. These results are consistent with the analytical results of Happel and Brenner discussed earlier. Note that some experiments[50] show two-sphere flows in which the centre-to-centre distance is not constant; however, this is probably an indication of the presence of inertia, which can lead, for example, to the 'kissing and tumbling' phenomenon observed in dynamical simulations at *non-zero* Reynolds numbers.[25]

The relative sharpness of the bounds of Table VII can also be understood on physical grounds. For instance, the lower bound is sharper than the upper bound because in the original flow the spheres are close enough that blocking the nip region—creating a dumb-bell—does not affect the mesoscale flow

substantially. This argument also explains why the lower bound is sharpest for the case in which the line of centres is aligned with gravity; intuitively, the nip region should be one of relatively low viscous dissipation in this configuration. Of course, the lower bound will also become sharper as the particles get closer together. Note, however, that when analysing a mesoscale-cell with many particles at high concentrations, the nip region between two close neighbours can still be a region of relatively high viscous dissipation if, owing to the particle distribution, fluid is 'forced' to flow through the nip region; clearly in this case the lower bound will not be as sharp.

Lastly, we close with an experiment with three spheres in a mesoscale cube to demonstrate that our numerical simulation can produce the relative motion of the particles. Figure 14 shows the surface mesh of the geometry we analyse, which consists of three spheres of diameter $d = 0{\cdot}1$ on the $y_3 = 0{\cdot}5$ plane; spheres 1 and 3 lie on a $y_2 = \text{const.}$ plane $0{\cdot}4$ units apart, while sphere 2 is positioned halfway between the first two but at $y_2 = \text{const.} - 0{\cdot}10$. As seen in Table VIII, spheres 1 and 3 fall down and towards each other while counter-rotating, while sphere 2 falls straight down at a higher settling speed than the other two spheres. It is important that our sedimentation formulation allows for relative motion of the particles, since this is an essential feature of real sedimenting suspensions.

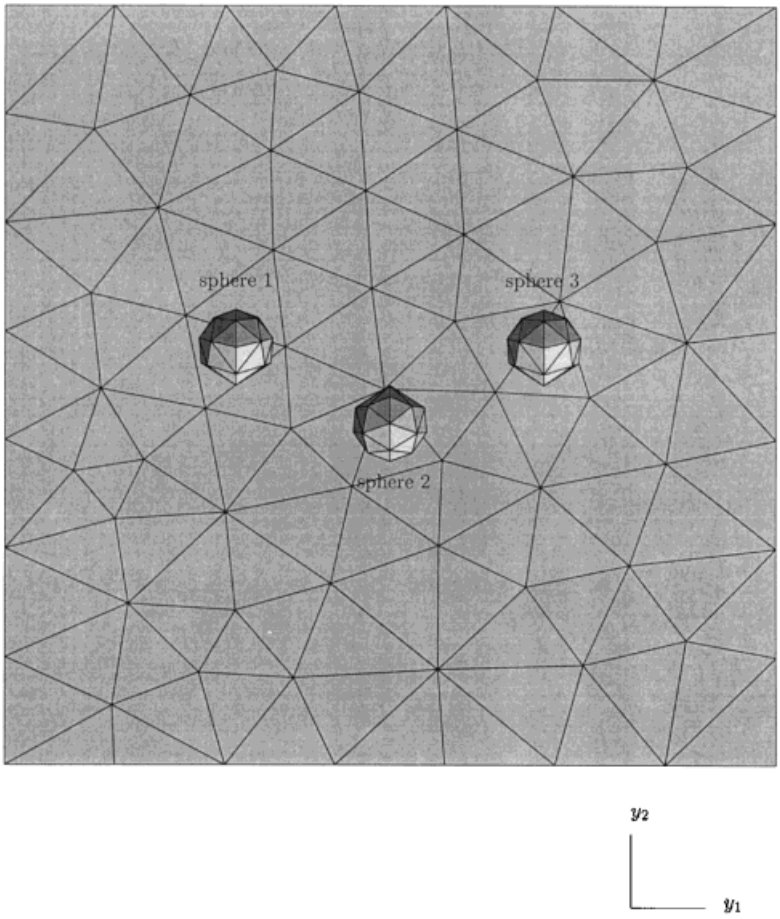

Figure 14. Sedimentation of three spheres in a mesoscale cell: surface meshes of spheres and one face of mesoscale cell

Table VIII. Translational and rotational degrees of freedom of three spheres falling in a mesoscale cube for the case described in the text and depicted in Figure 14

k	$(U_1)_k$	$(U_2)_k$	$(U_3)_k$	$(R_1)_k$	$(R_2)_k$	$(R_3)_k$
1	0·002954	−0·04860	—	—	—	−0·006537
2	—	−0·05423	—	—	—	—
3	−0·002953	−0·04866	—	—	—	0·006348

Future work should investigate random inclusion distributions by incorporating statistical analysis and parallel processing as described by Cruz *et al.*;[32] consider the moderate-Reynolds-number inertial flows often found in fluidized beds, as described in Reference 35; explicitly track the sedimentation particle trajectories in time as in Reference 25, thereby determining a self-consistent JPDF and associated settling speed; and study polydisperse and non-spherical inclusions.

ACKNOWLEDGEMENTS

We would like to thank Professor J. Peraire of M.I.T. for making his mesh generation package FELISA available to our project. This work was supported by DARPA and the ONR through Grant N00014-91-J-1889. In addition, one of us (M.E.C.) would like to acknowledge the support of the Brazilian Council for the Development of Science and Technology (CNPq).

REFERENCES

1. A. E. Scheidegger, *The Physics of Flow through Porous Media*, 3rd edn, University of Toronto Press, Toronto, 1974.
2. G. K. Batchelor, 'Transport properties of two-phase materials with random structure', *Ann. Rev. Fluid Mech.*, **6**, 227–255 (1974).
3. S. Kim and S. J. Karrila, *Microhydrodynamics: Principles and Selected Applications*, Butterworth–Heinemann, Boston, MA, 1991.
4. M. Ungarish, *Hydrodynamics of Suspensions: Fundamental of Centrifugal and Gravity Separation*, Springer, Berlin, 1993.
5. R. H. Davis and A. Acrivos, 'Sedimentation of noncolloidal particles at low Reynolds numbers', *Ann. Rev. Fluid Mech.*, **17**, 91–118 (1985).
6. H. L. Weissberg and S. Prager, 'Viscous flow through porous media, III, Upper bounds on the permeability for a simple random geometry', *Phys. Fluids*, **13**, 2958–2965 (1970).
7. J. Rubinstein and S. Torquato, 'Flow in random porous media: Mathematical formulation, variational principles, and rigorous bounds', *J. Fluid Mech.*, **206**, 25–46 (1989).
8. S. Torquato, 'Random heterogeneous media: microstructure and improved bounds on effective properties', *Appl. Mech. Rev.*, **44**, 37–76 (1991).
9. R. Hill and G. Power, 'Extremum principles for slow viscous flow and the approximate calculation of drag', *Q. J. Mech. Appl. Math.*, **9**, 313–319 (1956).
10. J. B. Keller, L. A. Rubenfeld and J. E. Molyneux, 'Extremum principles for slow viscous flows with applications to suspensions', *J. Fluid. Mech.*, **30**, 97–125 (1967).
11. H. F. Weinberger, ' Variational properties of steady fall in Stokes flow', *J. Fluid Mech.*, **52**, 321–344 (1972).
12. R. H. Davis and K. H. Birdsell, 'Hindered settling of semidilute monodisperse and polydisperse suspensions', *AIChE J.*, **34**, 123–129 (1988).
13. S. Yesilyurt, C. K. Ghaddar, M. E. Cruz and A. T. Patera, 'Bayesian-validated surrogates for noisy computer simulations; application to random media', *SIAM J. Sci. Comput.*, **17**, 973–992 (1996).
14. S. Kim and R. T. Mifflin, 'The resistance and mobility functions of two equal spheres in low-Reynolds-number flow', *Phys. Fluids*, **28**, 2033–2045 (1985).
15. G. K. Batchelor, 'Sedimentation in a dilute dispersion of spheres' , *J. Fluid. Mech.*, **52**, 245–268 (1972).
16. P. G. Saffman, 'On the settling speed of free and fixed suspensions', *Stud. Appl. Math.*, **52**, 115–127 (1973).
17. A. A. Zick and G. M. Homsy, 'Stokes flow through periodic arrays of spheres', *J. Fluid Mech.*, **115**, 13–26 (1982).
18. A. S. Sangani and A. Acrivos, 'Slow flow through a periodic array of spheres', *Int. J. Multiphase Flow*, **8**, 343–360 (1982).
19. H. C. Brinkman, 'A calculation of the viscous force exerted by a flowing field on a dense swarm of particles', *Appl. Sci. Res. A*, **1**, 27–34 (1947).
20. G. J. Kynch, 'A theory of sedimentation', *Trans. Faraday Soc.*, **48**, 166–176 (1952).

21. J. F. Brady and G. Bossis, 'Stokesian dynamics', *Ann. Rev. Fluid Mech.*, **20**, 111–157 (1988).
22. J. F. Brady, R. J. Phillips, J. C. Lester and G. Bossis, 'Dynamic simulation of hydrodynamically interacting suspensions', *J. Fluid Mech.*, **195**, 257–280 (1988).
23. A. J. C. Ladd, 'Hydrodynamic transport coefficients of random dispersions of hard spheres', *J. Chem. Phys.*, **93**, 3484–3494 (1990).
24. A. J. C. Ladd, 'Dynamical simulations of sedimenting spheres;, *Phys. Fluids A*, **5**, 299–310 (1993).
25. J. Feng, H. H. Hu and D. D. Joseph, 'Direct simulation of initial value problems for the motion of solid bodies in a Newtonian fluid. Part 1. Sedimentation', *J. Fluid Mech.*, **261**, 95–134 (1994).
26. A. Dasgupta, T. I. -P. Shih, K. P. Kundu and J. M. Deur, 'Flow past arrays of spherical particles at low to intermediate Reynolds numbers', *J. Fluid Mech.*, submitted.
27. S. J. Karrila, Y. O. Fuentes and S. Kim, 'Parallel computational strategies for hydrodynamic interactions between rigid particles of arbitrary shape in a viscous fluid', *J. Rheol.*, **33**, 913–947 (1989).
28. M. S. Ingber and D. E. Womble, 'Hindered settling computations using a parallel boundary element method', in S. Kim, G. Karniadakis and M. K. Vernon (eds), *Parallel Computing in Multiphase Flow Systems Simulations*, FED Vol. 199, ASME, New York, 1994, pp. 53–59.
29. D. H. Rothman, 'Cellular-automaton fluids: a model for flow in porous media; *Geophysics*, **53**, 509–518 (1988).
30. M. E. Cruz and A. T. Patera, 'A parallel Monte-Carlo finite-element procedure for the analysis of multicomponent random media', *Int. j. numer. meth. engng.*, **38**, 1087–1121 (1995).
31. M. E. Cruz, C. K. Ghaddar and A. T. Patera, 'A variational-bound nip-element method for geometrically stiff problems; application to thermal composites and porous media', *Proc. R. Soc. Lond. A*, **449**, 93–122 (1995).
32. M. E. Cruz, C. K. Chaddar and A. T. Patera, 'Parallel simulation of multicomponent random media', in S. Kim, G. Karniadakis and M. K. Vernon (eds), FED Vol. 199, ASME, New York, 1994, pp. 1–9.
33. M. Pedercini, 'Variational-bound finite-element methods for three-dimensional low-Reynolds-number porous media and sedimentation flows', *M.S. Thesis*, Massachusetts Insitute of Technology, Cambridge, MA, 1995.
34. C. K. Ghaddar, 'Parallel analytico-computational methods for multicomponent media: application to thermal composites and porous media flows', *Ph.D. Thesis*, Massachusetts Institute of Technology, Cambridge, MA, 1994.
35. C. K. Ghaddar, 'On the permeability of unidirectional fibrous media: a parallel computational approach', *Phys. Fluids*, **7**, 2563–2589 (1995).
36. M. E. Cruz, 'A parallel Monte-Carlo partial-differential-equation procedure for the analysis of multicomponent random media', *Ph.D. Thesis*, Massachusetts Institute of Technology, Cambridge, MA, 1993.
37. D. J. Jeffrey and A. Acrivos, 'The rheological properties of suspensions of rigid particles', *AIChE J.*, **22**, 417–432 (1976).
38. M. D. Gunzburger, *Finite Element Methods for Viscous Incompressible Flows: A Guide to Theory, Practice, and Algorithms*, Academic, San Diego, CA, 1989.
39. H. Kardestuncer (ed.), *Finite Element Handbook*, McGraw-Hill, New York. 1987.
40. Y. Maday, D. Meiron, A. T. Patera and E. M. Rønquist, 'Analysis of iterative methods for the steady and unsteady Stokes problem: application to spectral element discretizations', *SIAM J. Sci. Comput.*, **14**, 310–337 (1993).
41. G. H. Golub and C. F. Van Loan, *Matrix Computations*, 2nd edn, Johns Hopkins University Press, Baltimore, MD, 1989.
42. J. Peiró, J. Peraire and K. Morgan, *FELISA SYSTEM Reference Manual*, Computational Aerospace Sciences Laboratory/Aeronautics Department, MIT, 1993.
43. O. C. Zienkiewicz and R. L. Taylor, *The Finite Element Method*, Vol. 1, 4th edn, McGraw-Hill, London, 1989.
44. G. Strang and G. J. Fix, *An Analysis of the Finite Element Method*, Prentice-Hall, Englewood Cliffs, NJ, 1973.
45. G. Anagnostou, Y. Maday, C. Mavriplis and A. T. Patera, 'On the mortar element method: generalizations and implementation', in T. F. Chan, R. Glowinski, J. Periaux and O. B. Widlund (eds), *Domain Decomposition Methods for Partial Differential Equations, SIAM, Philadelphia, PA, 1990.*
46. J. F. Davidson, R. Clift and D. Harrison, *Fluidization*, 2nd edn, Academic, London, 1985.
47. J. Happel and H. Brenner, *Low Reynolds Number Hydrodynamics*, Martinus Nijhoff, The Hague, 1983.
48. G. I. Taylor, *Low Reynolds Number Flows*, Film, Encyclopaedia Britannica Educational Corp., Chicago, IL.
49. R. L. Panton, *Incompressible Flow*, Wiley, New York, 1984.
50. K. O. L. F. Jayaweera, B. J. Mason and G. W. Slack, 'The behaviour of clusters of spheres falling in a viscous fluid. Part 1. Experiment', *J. Fluid Mech.*, **20**, 121–128 (1964).

